RELATIONSHIP BETWEEN NEARLY COINCIDENT SPIKING AND COMMON EXCITATORY SYNAPTIC INPUT IN MOTOR NEURONS.

by

Marco Arieli Herrera-Valdez

A Dissertation Submitted to the Faculty of the

GRADUATE INTERDISCIPLINARY PROGRAM IN PHYSIOLOGICAL SCIENCES

In Partial Fulfillment of the Requirements
For the Degree of

DOCTOR OF PHILOSOPHY

In the Graduate College

THE UNIVERSITY OF ARIZONA

2 0 0 8

THE UNIVERSITY OF ARIZONA
GRADUATE COLLEGE

As members of the Final Examination Committee, we certify that we have read the dissertation prepared by Marco Arieli Herrera-Valdez
entitled Relationship between nearly coincident spiking and common excitatory synaptic input in motor neurons.
and recommend that it be accepted as fulfilling the dissertation requirement for the Degree of Doctor of Philosophy.

Date: August 28, 2008
Andrew J. Fuglevand

Date: August 28, 2008
Richard B. Levine

Date: August 28, 2008
Jean Marc Fellous

Final approval and acceptance of this dissertation is contingent upon the candidate's submission of the final copies of the dissertation to the Graduate College.

I hereby certify that I have read this dissertation prepared under my direction and recommend that it be accepted as fulfilling the dissertation requirement.

Date: August 28, 2008
Dissertation Director: Andrew J. Fuglevand

STATEMENT BY AUTHOR

This dissertation has been submitted in partial fulfillment of requirements for an advanced degree at The University of Arizona and is deposited in the University Library to be made available to borrowers under rules of the Library.

Brief quotations from this dissertation are allowable without special permission, provided that accurate acknowledgment of source is made. Requests for permission for extended quotation from or reproduction of this manuscript in whole or in part may be granted by the head of the major department or the Dean of the Graduate College when in his or her judgment the proposed use of the material is in the interests of scholarship. In all other instances, however, permission must be obtained from the author.

SIGNED: _____

Marco Arieli Herrera-Valdez

ACKNOWLEDGEMENTS

This work would have not been possible without the help I received, in many different shapes, forms and capacities, from many people that I am hoping to acknowledge without omissions. More or less, in chronological order of appearance: Larry Grove, Jan Wehr, Joe Watkins, Emiliano Gallaga, Gillian Newell, Canek Fuentes, Jesus Espinola, Doug Ulmer, Rick Levine, Raphael and Jolene Gruener, Bob Gatenby, John Hildebrand, Tom Christensen, Hong Lei, Carolina Reisenman, Pablo Guerenstein, Andrew Dacks, Norm Davis, Andrea Yool, Joceline Lega, Silvia Madrid, Anak and Ann Shresta David Morales, Janis Burt, Ron Lynch, Hedween Brooks, Elton and Renata Migliati, Holly Lopez, Kathalin Gothard, Jose Ek, Peter Lipa, Pawel and Monika Musialp, Masami Tatsuno, Susana Rossi, Diano Marrone, Jean Marc Fellous, Carol Barnes, Bruce McNaughton, Kevin Spitler, Leslie Schimanski, Michael Montgomery, Luann Snyder, Michelle Carroll, Sharon Crook, Carsten Duch, Li-Wei Chow, Ann Revill and Jason Worrell. Special thanks to members of my (extended) family, Erin McKiernan (the wife), John and Maggie McKiernan, Alex Thome and Kate Larsen, Victor Ramirez, Anuar Jose, Fernando y Cristina Rosete, Bob Condon, Erendira Valdez, Ignacio Herrera, Cesar Herrera, Joel Valdez, Irma Valdez.

The science and math in this dissertation were heavily influenced by the work of people like Nancy Kopell, William Bialek, Bard Ermentrout, David Terman, Greg Smith, Terry Sejnowski, Maxim Bazhenov, Steve Baer, John Rinzel, Eugene Izhikevich, C. Koch, Idan Segev, Alain Destexhe, Michael Rudolph, Carlos Brody, and many others.

Finally, I would like to thank my advisor Andy Fuglevand. From my interactions with Andy I learned many things about myself and about what I want to become. A solid scientist like Andy reads the old and new literature, is patient, consistent , and honest to himself. Andy does every single one of those things without hessitating, he is willing to reconsider his positions without putting his ego on the way.

To all of you, thank you.

DEDICATION

To all those who are willing to question the dogma.

Marco Arieli Herrera-Valdez,

Tucson, Arizona,

November 2008.

TABLE OF CONTENTS

TABLE OF CONTENTS – Continued

List of Figures

List of Figures – *Continued*

List of Tables

ABSTRACT

Abstract: The activities of pairs of mammalian motor neurons (MNs) receiving varying degrees of common excitatory synaptic input were simulated to study the relationship between nearly-coincident spiking and common excitatory drive. The somatic membrane potential of each MN was modeled using a single compartment model. Each MN was modeled to receive synaptic contacts from hundreds of pre-synaptic fibers. The percentage of pre-synaptic fibers that diverged to supply both MNs of a pair with common synaptic input could be varied from 0 (no common inputs) to 100% (all common inputs). Spikes trains on separate pre-synaptic fibers were independent of one another and were modeled as realizations of renewal processes with mean firing rates (10 - 50 Hz) resembling that associated with supra-spinal input. Maximum synaptic conductances and time constants were varied across synapses to match experimentally observed somatic EPSPs. The number of active pre-synaptic fibers to each MN was adjusted in order that the firing rates of MNs were between 8 and 15 Hz. For each common input condition, 100 s of concurrent spiking activity of the MNs was used to construct cross-correlation histograms. The sizes of the central peaks in the histograms were quantified using both the k (Ellaway and Murthy 1985) and CIS (Nordstrom et al. 1992) indices of synchrony. Monotonically increasing linear relationships between the proportion of common synaptic input and the magnitude of synchrony were observed for both indices. For example, the model predicted that 10% common input would yield a CIS value of 0.27 whereas 100% common input would yield a CIS value of 1.5. These values are within the range of values observed experimentally. These results, therefore, provide a means to translate measures of nearly-coincident spiking into plausible renditions of synaptic connectivity.

Chapter 1

Introduction

1.1 Introduction

Tasks like breathing, balancing, locomoting, and grasping are accomplished by the coordinated contraction of teams of muscles. Each muscle, in turn, is comprised of tens of thousands of muscle fibers. In normal conditions in vertebrates, each fiber is innervated by one motor neuron (MN) and a single MN may innervate tens to hundreds of muscle fibers. A MN together with the muscle fibers it supplies constitute the output element of the nervous system and is referred to as a *motor unit*. The few hundred motor units that comprise a single muscle is called a *pool*. How the central nervous system coordinates the activities of motor units across a wide range of behaviors is poorly understood and remains an area of intense research. The main goal of this dissertation, therefore, was to create a theoretical framework to enable accurate predictions of synaptic connectivity within and across pools of motor neurons based on the spiking patterns of concurrently recorded motor units.

During the execution of many tasks, a subset of the recruited MNs fire a significant number of nearly-coincident spikes (Dietz et al., 1976; Sears and Stagg, 1976). That is, a fraction of the spikes from such neurons occurs within a few milliseconds of one another and the number of nearly-coincident spikes is more than would be predicted if the MNs fired independently (Sears and Stagg, 1976; Kirkwood, 1979; Kirkwood et al., 1982a). Nearly-coincident spiking is measured in terms of the relative timing of spikes from the two neurons by calculating the raw *correlation function* of their spike trains. These correlation functions measure the relative frequency with which the event of observing a spike from one of the neurons (called the reference neuron) occurs h time units away from a spike in the second neuron (called response neuron). In other words, these correlation functions yield counts of *joint*

spiking. The graph of the correlation function is called *correlogram* (see Fig. 1.1 and Methods). Significant nearly-coincident spiking occurs when there is a peak around time-delay zero (Fig. 1.1A). The duration of nearly-coincident spiking is usually regarded as the size of the time interval containing the peak. Pronounced peaks in a correlogram suggest that the two spike trains are not independent whereas "flat" correlograms are usually considered to indicate of independent spiking. The lack of independence could be due to various factors including direct or indirect synaptic coupling between the two neurons and/or correlated changes in the firing rates of the two spike trains Brody (1999a); de la Rocha et al. (2007).

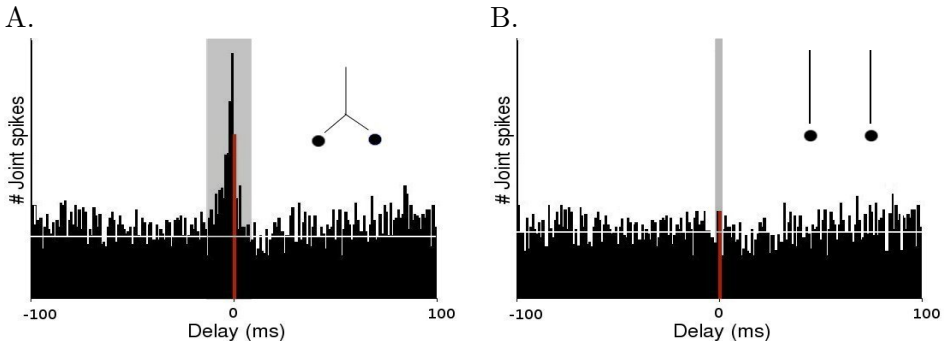

Figure 1.1: Correlograms from two different spike trains. The red line shows the count for perfectly coincident, hence synchronous spikes (up to resolution). The white horizontal line shows a baseline that estimates the counts that would result if the two spike trains were independent. The shaded regions mark the portions of the correlogram containing the nearly-coincident spike counts delimited by finding the largest connected interval around time-delay zero for which the counts are larger than a baseline. The insets show a schematic representation of a possible scenario of presynaptic inputs that could explain the shape of the correlogram. **A.** Correlogram suggesting a clear departure from independence in the two spike trains. **B.** Correlogram indicative of independent spike trains. As expected, the region of nearly-coincident spikes for the case in which there is a clear peak in the correlogram (A) is wider than the case for the "flat" correlogram.

In their seminal report, Sears and Stagg (1976) advanced the hypothesis that nearly-coincident spiking results from the joint occurrence of unitary post-synaptic potentials from common stem presynaptic fibers (see inset Fig. 1.1A). A few years later, Kirkwood et al. (1982a) elaborated further on this hypothesis and postulated that if nearly-coincident spiking lasts less than 10 ms, then excitation likely

originates from common stem presynaptic fibers, whereas if the duration of nearly-coincident spiking is longer (*ca.* 20-30 ms), then excitatory drive likely arises from separate axons exhibiting correlated firing.

The experimental evidence in support of the above hypothesis is indirect. Yet, most researchers have adopted the interpretation that short-lasting (<10 ms) central peaks in correlograms are indicative of common excitatory input (Fig. 1.1A). Conversely, flat correlograms are usually taken to indicate lack of common input (Fig. 1.1B). However, there are potential problems with these interpretations that are largely related to the absence of a quantitative foundation upon which to evaluate the shape and size of a correlogram. For instance, a "flat" correlogram may not necessarily mean that the two neurons under study receive no input in common. Similarly, it is currently impossible to make quantitative inferences about the levels of common excitatory input received by two neurons that exhibit a central peak in their correlogram. To make matters more complicated, two neurons with rhythmic output of similar frequencies (say, 10 Hz each) are likely to have a correlogram containing periodic peaks of non-negligible amplitudes in spite of a lack of common input at all.

Therefore, for this dissertation, I developed a model of simultaneously spiking neurons in which the number of common excitatory inputs, their rates of spiking, and their synaptic efficacy could be controlled. Such a model was used to identify sources of correlation in MN spiking and were related to possible connectivity schemes (Brody, 1999b; Nykamp, 2003). In addition, the model was used to assess the accuracy of the current analyses methods.

The work done for this dissertation had the following specific aims:

1. To assess the possibility that nearly-coincident spiking can be observed in pairs of uncoupled MNs receiving common but otherwise uncorrelated, synaptic excitatory input.

2. To characterize the strength of nearly-coincident spiking for different levels of common excitatory input by measuring the size and width of central peaks

in correlograms using the experimentally deployed indices k' (Ellaway and Murthy, 1985) and common input strength (CIS) (Nordstrom et al., 1992).

3. To characterize how the duration of nearly-coincident spiking varies, if at all, as a function of the number of common excitatory inputs received by MNs. This aim required the development of a novel analysis method to allow reliable identification of small peaks in correlograms.

4. To characterize nearly-coincident spiking as a function of common excitatory input in pairs of MNs (a) with different levels of excitability (*i.e.,* as would occur when recording from motor units of different recruitment thresholds); (b) receiving different levels of excitatory drive.

The construction of a computationally efficient, yet physiologically relevant model of spinal MNs receiving realistic synaptic input and which exhibited membrane potential dynamics that resembled those observed experimentally was required to address the specific issues mentioned above. As a consequence, a major undertaking associated with this dissertation was the development and validation of such a model.

The following chapters describe the background, approach, and outcome of simulations to address these aims. Chapter 2 provides a brief literature overview of mammalian MNs, motor units, the general organization of synaptic input to MNs, MN electrophysiology, and nearly-coincident spiking. Chapter 3 describes various methods to analyze spike trains and chapter 4 presents different methods used to model spiking activity in excitable cells leading to a full description of the model used in this dissertation to simulate MN behavior. The model developed in chapter 4 is applied in chapter 5 to characterize the relationship between motor neurons receiving common excitatory synaptic drive and nearly-coincident spiking under a variety of conditions. A summary, discussion, and proposal for future directions of this dissertation work are presented in chapter 6.

Chapter 2

Literature review

Movement is the result of muscle contraction, which, in turn, is controlled by *motor neurons* (MNs). MNs that control facial muscles and the tongue are located in the brain stem, whereas MNs supplying limb skeletal muscles are located in logitudinally-oriented nuclei in the ventral horn of the spinal cord. Individual muscles are composed of tens of thousands of muscle fibers. In normal conditions in adult mammals, each muscle fiber is innervated by a single MN. In contrast, each MN makes synaptic contact with tens to thousands of muscle fibers. A MN together with the muscle fibers it innervates is called a *motor unit*. Each muscle, in turn, is controlled by a team of a few hundred motor neurons, ofter referred to as the MN *pool* for the muscle.

Neurons and skeletal muscle fibers are excitable, which means that their membrane is equipped with proteins that mediate electrical signaling in the form of all-or-none electrical pulses called action potentials (APs), or spikes. A very important property of motor units is that APs from the commanding MN are followed one-for-one by APs in all the muscle fibers in the unit. Therefore, it is possible to track motor neuron activity by recording in the periphery.

The following paragraphs contain a brief overview of the properties of motor neurons followed by a review of the synaptic inputs to MNs. The last sections discuss possible links between the simultaneous spiking in MNs and the synaptic organization of supraspinal inputs to MNs.

2.1 Spiking properties of motor neurons under current injection.

The typical behavior displayed by mammalian spinal MNs under current injection is described in the following paragraphs (Calvin and Schwindt, 1972; Kernell, 2006)

and illustrated in Figs. 2.1 and 2.2.

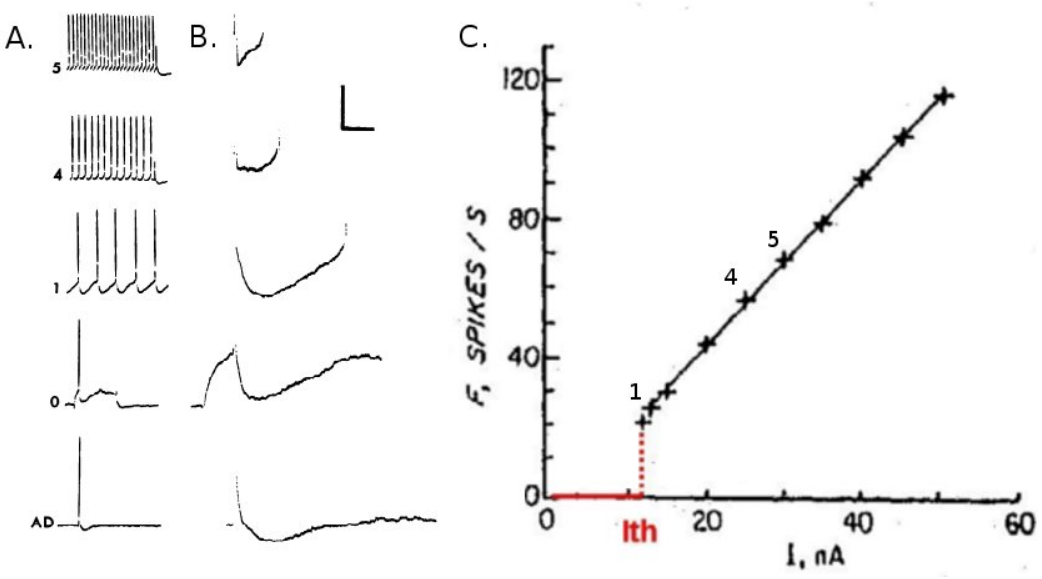

Figure 2.1: Typical firing behavior of mammalian MNs under current injection. **A.** Responses to different levels of current injection in a spinal motor neuron from a cat (Granit et al., 1963; Calvin and Schwindt, 1972). The subscripts on the left of each trace indicate different pulses used to stimulate the MN. *AD* is the trace that results from a short pulse of current sufficiently large to trigger one action potential. The numbers 0-5 indicate long pulses of increasing amplitudes, also noted in part C. **B.** Trajectories of the membrane potential between spikes magnified from the records in **B**. Calibrations for **A** and **B**: 40 mV, 80 ms in **B**; 10 mV. **C.** Current-frequency relationship displayed by a spinal mammalian MNs. The minimum current amplitude required to trigger sustained spiking is marked as "I_{th}".

- MNs have a *stable membrane potential* in the absence of stimulation (Kernell, 1965a). The minimal current amplitude necessary to evoke an AP with a short pulse (*rheobase*) normally is between 5 and 20 nA (Fig. 2.1A-B lower traces). MNs do not have a "hard current threshold" in the sense that a single action potential can be triggered at different current levels depending on the rate of rise and duration of current injection (not shown).

- After firing a single spike, the membrane potential undergoes an *after-hyperpolarization* that lasts between 80 and 150 ms with an amplitude between 5 and 10 mV (Kernell, 1965b). The return trajectory of the membrane

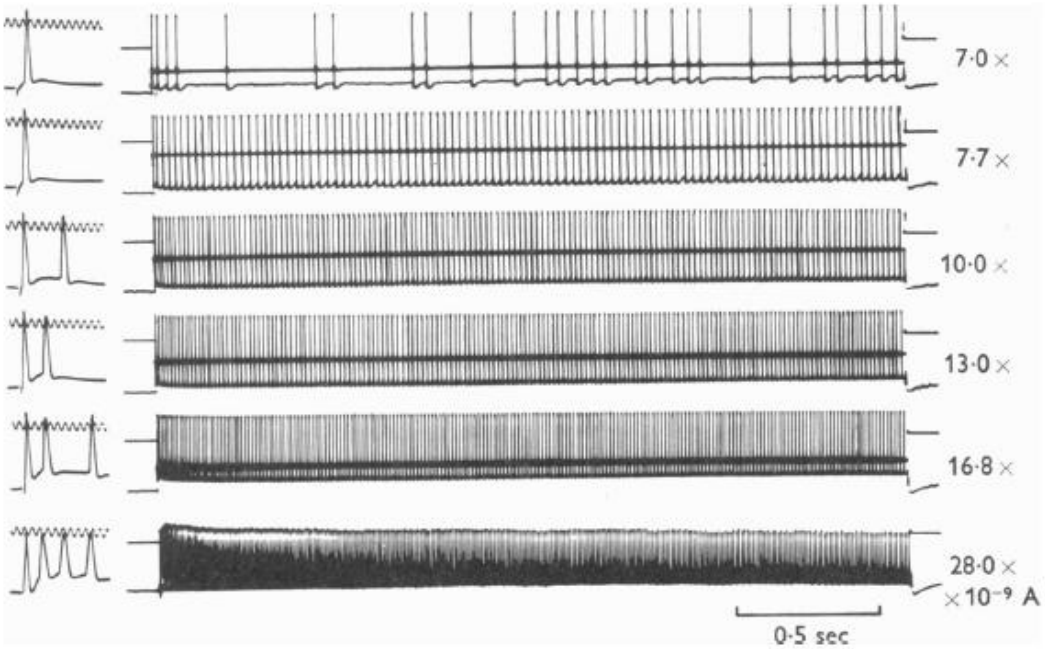

Figure 2.2: Repetitive firing of mammalian MNs under current injection from Granit et al. (1963). The spikes in the left column show the first discharges of the cell in response to the stimulus pulse. The middle column shows the repetitive MN firing for different levels of current amplitude. The numbers in the right column are the amplitudes (in nA) of the stimulation pulses. Note the increase in firing frequency for larger current amplitudes and the different amplitudes of APs in the last recorded trace.

potential to rest after the downstroke of a spike is often monotonic as shown in the bottom traces in Fig. 2.1B-C.

- For square current pulses of long duration ($>$ 200 ms) there is a threshold current, I_{th}, at which MNs display sustained periodic firing, with an initial frequency of sustained spiking that is not arbitrarily small (Granit et al., 1963). If the injected current is large enough, the first few spikes occur in a brief burst of two, three or perhaps more spikes. After this brief burst, the firing rate of the neuron undergoes a slow adaptation toward periodic firing (Bawa and Calancie, 1983) (Fig. 2.1B). In consequence, the current-frequency relationship is discontinuous, displaying zero frequency for an interval of injected currents and jumping to a nonzero frequency at the minimal current

that elicits sustained firing (Fig. 2.1C). The ratio between the rheobase current and the repetitive spiking threshold I_{th}/I_{rheo} is about 1.5. Note also that MN spikes can be of different sizes as can be seen in the last recorded trace of Fig. 2.2.

2.2 Motor neurons and their presynaptic inputs

MNs receive synaptic input from sensory afferents, spinal interneurons, and from descending axons that originate in the brainstem and cerebral cortex (Kernell, 2006). While the relationship between the activities of sensory afferents and postsynaptic responses in MNs has been studied extensively. Much less is known about the synaptic organization of inputs to MNs from supraspinal and spinal neurons.

Somatosensory *afferent axons* carry information originating in muscles, tendons, skin, and joints into the central nervous system. The cell bodies of peripheral afferents for body regions below the neck are located in the dorsal root ganglia, adjacent to the spinal cord. Axon collaterals from many of these sensory afferents make synaptic connections with MNs and interneurons located within the same, as well as adjacent spinal segments (Kernell, 2006). Two nomenclatures are used to classify somatosensory axons based on the tissue from which they arise: a Roman numeral system for muscle afferents and a combined Latin-Greek lettering system for skin afferents. Within each system, axons are classified into groups depending on their thickness and myelination. For example, types I-III are thicker than the unmyelinated type IV muscle afferents. The two thickest types I and II carry information related to muscle length and force and arise from muscle spindles and Golgi tendon organs. An individual Ia axon arising from the primary ending of a muscle spindle makes direct excitatory synaptic connections with virtually every MN innervating their originating muscle (homonymous), as well as a large proportion of the MNs innervating different muscles (heteronymous) with complementary or synergistic actions to the homonymous muscle (Mendell and Henneman, 1971). In addition to exciting MNs controlling synergistic muscles, type Ia afferents also excite inhibitory

interneurons that innervate MNs controlling antagonistic muscles (Jankowska and Roberts, 1972). The thinner types III and IV muscle afferents carry more diverse types of information, including nociceptive, mechanoceptive (*e.g.,*pressure-related signals) and chemoceptive information (*e.g.,*metabolically-evoked changes in the extracellular environment of muscles and release of chemicals following tissue damage). Such sensory afferents make excitatory connections with spinal local interneurons which in turn make direct or indirect contacts with MNs.

Spinal interneurons integrate information from supraspinal, spinal and peripheral inputs (Baldissera et al., 1981; Jankowska, 1992) and transfer it to MNs. The dendrites and axon collaterals of spinal interneurons may span more than one spinal segment, as well as dorsal and ventral portions of the spinal cord. In addition, there are a few spinal interneurons that extend neurites to communicate with contralateral cells (Kandel et al., 2000). Synaptic input from spinal interneurons onto MNs can be excitatory or inhibitory. Consequently, the spiking activity of interneurons may have different effects on the activity of muscles through their influence on MN activity (Perlmutter et al., 1998).

The sites of origin of *descending tracts* include premotor, primary and somatosensory motor cortices, vestibular nuclei and other brainstem sources (Kandel et al., 2000). Axons comprising these descending tracts target interneurons in the dorsal horn and intermediate gray matter of the spinal cord. In addition, some descending axons, particularly those of cortical origin in primates, project to the ventral horn of the spinal cord to make direct synaptic contacts with MNs innervating an individual muscle and may also extend collaterals that contact MNs supplying different muscles (Asanuma et al., 1979; Shinoda et al., 1981; Lawrence et al., 1985). Supraspinal inputs, therefore, constitute another source of common, branched input to MNs. The *corticospinal tracts* in higher primates are of particular importance because they are believed to be the main source of synaptic drive to spinal MNs during voluntary motor behaviors (Penfield and Boldrey, 1937; Porter and Lemon, 1993; Romo and Salinas, 1999).

MNs respond to monosynaptic input from the same input axon with post-

synaptic potentials of different amplitudes. Each input cell makes several synapses onto its target MN, with each synapse having a different efficacy as suggested by experiments stimulating peripheral neurons (Redman and Walmsley, 1983a), inhibitory interneurons (Jankowska and Roberts, 1972), rubrospinal cells (Shapavalov et al., 1971) and corticospinal pyramidal neurons (Jankowska et al., 1975). For example, there are anatomical and physiological data obtained from stimulation of single Ia afferents in cats (Redman and Walmsley, 1983a) that show clearly that a single Ia afferent makes multiple synapses onto a single MN, triggering somatic excitatory postsynaptic potentials (EPSPs) of different amplitudes. The efficacy of each of the synapses of Ia afferents onto MNs was studied by Walmsley et al. (1988) who demonstrated that each synapse had its own probability of transmitter release, as reflected in the distribution of amplitudes for the composite EPSPs recorded in response to spikes from a single Ia afferent.

2.3 Nearly-coincident spiking in relation to synaptic input to MNs

An indirect way to extract information about synaptic connectivity within and across MN pools is to record simultaneous spiking activity in motor units in search for correlations. The one to one correspondence between APs in a MN and the fibers in its motor unit allows the study of MN spiking in response to synaptic input through extracellular recordings from easily accesible muscles. As mentioned previously, an important behavior displayed by some MNs during the execution of many motor tasks is that some of the recruited MNs display nearly-coincident spiking (Dietz et al., 1976; Sears and Stagg, 1976). That is, some of the spikes from the recruited neurons occur within a few milliseconds of one another more often than would be predicted if their spike trains were independent.

Nearly-coincident spiking has been observed in several vertebrate species (e.g. cats and primates including humans) in decerebrate (Connel et al., 1986), anesthetized and awake subjects (Sears and Stagg, 1976), during involuntary (Adams et al., 1989) and voluntary contractions (Datta et al., 1991), in isometric (Brem-

ner et al., 1991a; Datta and Stephens, 1990; Winges and Santello, 2004; Keen and Fuglevand, 2004; Hockensmith et al., 2005; McIsaac and Fuglevand, 2007) and non-isometric contractions (Semmler et al., 2002), as well as under different conditions of propioception (Garland and Miles, 1997). Further, nearly-coincident spiking occurs in MNs innervating different compartments within the same muscle (Datta and Stephens, 1990; Datta et al., 1991; Keen and Fuglevand, 2004; McIsaac and Fuglevand, 2007) and between ipsilateral (Bremner et al., 1991b; Hockensmith et al., 2005) muscles. In addition there are controversial, yet suggestive reports of near-coincident spiking in contralateral muscles during the execution of postural tasks (Gibbs et al., 1995) (but see (Mochizuki et al., 2005)). Importantly, physiological roles for nearly-coincident spiking in MNs in motor control have yet to be established. In fact, some theoretical (Yao et al., 2000), lesion, and functional studies (Kirkwood et al., 1982a,b) have linked nearly-coincident spiking to tremor, lack of dexterity, and arrhythmic contractions in muscles.

As mentioned earlier, Sears and Stagg (1976) advanced the hypothesis that nearly-coincident spiking results from the joint occurrence of unitary post-synaptic potentials from common stem presynaptic fibers. Indirect experimental evidence indicating that common excitatory synaptic input increases the occurrence of nearly-coincident spikes in MNs was first provided by Kirkwood and Sears (1978). In that study, Kirkwood and Sears (1978) showed that if a pair of MNs displays nearly-coincident spiking, transient depolarizations occur in the membrane potential of one of the MNs at the time of discharge the other MN. Such depolarizations were called *average common excitation* (ACE) and constitute the best evidence of the relationship between nearly-coincident spiking and the common synaptic excitatory drive to MNs. However, it has not been shown that ACE in two MNs recorded simultaneously result from activation of previously identified common presynaptic branches. A few years later, Kirkwood et al. (1982a) found that light anesthesia or polysynaptic activation of spindle afferents promoted increases in the width of central peaks in correlograms. If anesthesia levels were increased further (thus decreasing descending drive), the central peaks disappeared. However, if descending

excitatory drive to the recorded MNs was increased in the presence of mild levels of anesthesia, then the width of the central peaks decreased. Based on these findings Kirkwood et al. postulated that if near-coincident spiking lasts up to 10 ms, then excitation likely originates from common stem presynaptic fibers, whereas if nearly-coincident spiking is of longer duration (*ca.* 20-40 ms), then excitatory drive probably comes from separate inputs which themselves possess correlated activity. In view of the above findings, nearly-coincident spiking is regarded as a useful fingerprint of the underlying organization of synaptic input to MNs.

2.3.1 Experimental evidence of nearly-coincident spiking in relation to common input

Experimental work *in vivo* (Gilchrist and Mesche, 1997; Johnston et al., 1998) and *in vitro* (Ali et al., 1998) has been done to assess the existence of common input to pairs of cells. For instance, Gilchrist and Mesche and Johnston et al. have done intracellular pair recordings in the leech and in the moth, respectively, from neuromodulatory cells that show coactivation, and identified presynaptic sources explaining the joint-spiking observed in these cells. The experiments by Ali et al. (1998) involved slice intracellular recordings from basket and bistratified interneurons in the CA1 region of the hippocampus while simultaneously recording intracellularly from a pyramidal cell. In this case the time course of the membrane potentials in the three simultaneously recorded neurons was used to deduce a common presynaptic influence of pyramidal cells on the interneurons. The specific link between the input and output correlations in two neurons has also been studied in slice preparations *in vitro* by de la Rocha et al. (2007) and Markowitz et al. (2008). In these experiments, current input signals were injected into a pair of cells. The current signals had common and uncommon elements with respect to the cell pair. The correlations between the spike trains were measured and related to the correlation in the input currents. Two of the main conclusions of these experiments were that the correlation between the spikes in two neurons receiving common input will increase with the level of input correlation. The relationship between input and output correlation was quasi-linear.

In both cases the input-output correlation increased exponentially only when the input correlation values were larger than 0.8.

The level of common synaptic input in the motor system has only been investigated during fictive locomotion (Nielsen et al., 2005). In this case fictive locomotion patterns were induced in a decerebrate preparation. These experiments result in very small levels of nearly-coincident spiking, which led Nielsen et al. to conclude that the recorded MNs do not receive high levels of common input. The results suggest that nearly-coincident spiking in lumbar MNs does not play an important role in producing fictive locomotion and indirectly suggest that if any significant nearly-coincident spiking is observable in the whole-animal, it most be of cortical origin.

2.3.2 About the quantification and interpretation of nearly coincident spiking.

Sears and Stagg (1976) quantified nearly-coincident spiking using correlograms from pairs of MNs. The presence of a pronounced, central peak in the joint spike count plot reflects the occurrence of nearly-coincident spiking (Fig. 1.1). The current methodology to quantify the duration of near-coincident spiking relies on finding the width of the region of the central peak that lies above a baseline level (Fig. 1.1 shaded regions).

The most popular way to delimit the region of near-coincidence from joint spike count plots is called the "cumulative-sum method" (Ellaway, 1978). The cumulative sum method has been widely used in studies involving the spiking activity in motor units (Ellaway and Murthy, 1985; Kirkwood et al., 1982a; Nordstrom et al., 1992; Semmler et al., 2003; Keen and Fuglevand, 2004; Winges and Santello, 2004; McIsaac and Fuglevand, 2007). In brief, the cumulative sum method estimates a baseline count for the number of joint spikes by calculating the mean spike count outside the central region, labeled M in Fig. 2.3. A cumulative sum of the joint-spike counts after subtracting the baseline is then calculated as illustrated in Fig. 2.3. In those cases where there is a prominent peak, this central cumulative sum is expected to be flat before and after the peak, and increasing where the peak occurs. The

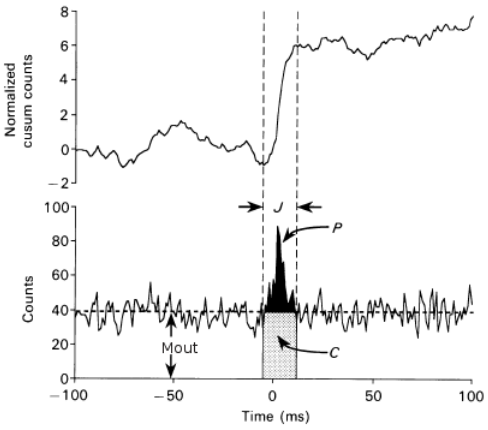

Figure 2.3: Peak detection in correlogram using Ellaway's cumulative sum. A central cumulative sum Ellaway (1978) is calculated relative to the mean M. If a central peak is present, the cumulative sum will display a significant increase. From Nordstrom et al. (1992).

peak is then delimited by the region where the cumulative sum undergoes a large increase. This method is reliable for cases in which the central region contains a prominent peak, but fails otherwise. In those cases where the peak is not prominent, the central region is often defined to be between -5 and 5 ms (see Sect. 3.3.2 for more details). Note that the cumulative sum method introduces two sources of error in the quantification of nearly-coincident spikes. First, the baseline may not be a good approximation for the correlation function that would be obtained if the trains were independent. Second, the central region is not well defined when peaks are not prominent.

Central peaks in correlograms may emerge for a pair of neurons for many reasons including, but not limited to similar excitability in the neurons or similar latencies in response to a common stimulus. Synaptic coupling, whether direct, indirect, chemical or electrical, could also give rise to central peaks in correlograms obtained from any pair of neurons. Uncommon, yet, correlated input to MNs could also give rise to nearly-coincident spiking (Brody, 1999a,b). As noted above, correlation functions are widely used to assess the occurrence, duration, and strength of nearly-coincident spiking. Moreover, the duration of nearly-coincident spiking has been used to make inferences about the synaptic organization of inputs to MNs. In view of the above observations, it is of critical importance to identify the possible causes for the emergence of nearly-coincident spiking and discard as many of those explanations as possible, especially if estimations about synaptic connections to MNs are to be

made based on joint spike counts. In addition, it is of crucial importance to have a reliable method to estimate the width of the peak region. Some experimental results that indicate possible sources of nearly-coincident spiking in MNs are reviewed next.

2.3.3 About the sources of nearly-coincident spiking

Several investigators (Kirkwood et al., 1982a,b; Baker et al., 1987) have reported that nearly-coincident spiking occurs in MN networks in which peripheral afferent input has been eliminated. In addition, Farmer et al. (1993) reported that nearly-coincident spiking is present in motor units that control intrinsic hand muscles in patients with lesions caudal but not rostral to the sections of the spinal cord that contain the MNs that command the motor unit. One strong suggestion from such results is that coupling between MNs through the spinal local network is not sufficient to cause nearly-coincident spiking (but see Kirkwood et al. (1982a)). These results are particularly important since they eliminate synaptic coupling (direct or indirect, provided by the local and afferent inputs) between MNs as a possible source of nearly-coincident spiking. As a consequence, correlated presynaptic inputs, common inputs to MNs, and similar excitability remain as the most likely candidates to explain the emergence of nearly-coincident spiking.

Two MNs with similar excitability may display similar firing rates under similar synaptic drive (Brody, 1999a). In this regard, Datta and Stephens (1990) reported that MN pairs with different recruitment thresholds display less nearly-coincident spikes when compared to neurons having the same recruitment threshold. Notably, MN pairs recruited at either low, or high range of forces, displayed stronger nearly-coincident spiking than MN pairs recruited at middle-range force levels, indicating that nearly-coincident spiking does not necessarily increase with excitability.

It is worth notice that others have not been able to corroborate these findings (Nordstrom et al., 1992). In addition, Nordstrom et al. showed that when the same pairs of units were made to fire at different rates, most of the commonly used indices of synchrony exhibited higher values when the motor units fired at lower rates. This interesting but counter-intuitive result directly contradicts theoretical predictions

made by de la Rocha et al. (2007). Nordstrom et al. also argued that such firing-rate dependence was an artifact of the method used to count nearly-coincident spikes and did not reflect an actual change in the extent of common synaptic drive. As such, Nordstrom et al. derived a new index of coincidence, called common input strength (CIS), that was insensitive to the effects of firing rate in their experiments. Nevertheless, the underlying relationship between firing rates of MNs and the degree of common synaptic input remains unresolved and controversial.

2.4 Overview.

The existing anatomical and physiological data from MNs justifies the study of nearly-coincident spiking in search for clues about the organization of synaptic inputs to spinal MNs. The technical difficulties that prevent the obtention of direct evidence in support of the hypotheses that nearly-coincident spiking results from common excitatory synaptic input calls for a theoretical approach to investigate possible schemes of connectivity and interactions between MNs and their targets. The existing models of nearly-coincident spiking are based on somewhat unrealistic assumptions about synaptic input to MNs (Binder and Powers, 2001; Lowery and Erim, 2005; Taylor and Enoka, 2004). For instance, Binder and Powers (2001) used a threshold crossing model with a single K^+ current that decayed exponentially to model MN excitability and common synaptic input was simulated by injecting a voltage-independent filtered signal (current) into model neurons. Lowery and Erim (2005) also used current injection to simulate common input. As has been shown by Kuhn et al. (2004), the firing frequency behaves differently when synaptic input is assumed to be voltage-dependent. Taylor and Enoka (2004) simulated the spiking activity of MNs, modeling the response to synaptic activation by assuming that the combination of several independent Poisson spike trains results in a Poisson spike train. One implication of this assumption was that the coefficient of variation of the interspike intervals of the model neuron was too high (close to 1), reflecting the statistic of the arrival times of the input spikes. The occurrence of

nearly-coincident spiking can be greatly affected by the coefficients of variation of the neurons involved.

Therefore, it is necessary to construct models of simultaneous spiking activity in MNs grounded on well established anatomical and physiological data. Modeling under these constrains provides physiologically relevant screening of several possible schemes of correlated activity and produce testable hypotheses for experiments. The theoretical work done for this dissertation enables the study of possible correlation schemes for synaptic input to MNs and relates them to experimentally deployed measures of nearly-coincident spiking. Theoretical results obtained with the models constructed here facilitate the study of the organization of synaptic input to MNs through their simultaneous spiking activity.

Chapter 3

Analysis of spike trains in the time domain

The following chapter describes general methods for quantification of spike trains. Spike rates, interspike intervals, and coefficients of variation are explained first, followed by a general description of methods to quantify simultaneous spiking activity in pairs of neurons. Particular emphasis is put on correlation functions and measures derived from them. The reason to do so is that the main interest in this dissertation is to quantify the occurrence of nearly-coincident spiking in pairs of motor units. Two methods to assess the existence and size of significant fluctuations in correlation functions will be described. The first method depends on the calculation of a cumulative sum (Ellaway, 1978). The second method is based on the search for the local extrema of the correlation function using a theoretical prediction of the correlation function that would result if the spike trains were independent as a baseline for separation. The calculations of the widely used indices of nearly-coincident spiking k' and CIS are explained in the last section. The results of these calculations are compared by using the cumulative sum method for peak detection and the correction for independence mentioned in previous paragraphs.

3.1 Spike trains: Definitions and basic quantification.

Assume that a record of membrane potential is sampled at time steps of size δ_t in the interval $[0, T]$. Assume also that all time quantities are in units of milliseconds (ms). The number of sample points in the recording is thus the integral part of $N_T = T/\delta_t$. The occurrence of spikes can usually be detected by setting a large enough threshold (Fig. 3.1). A sequence of spike times obtained this way is called a *spike train*.

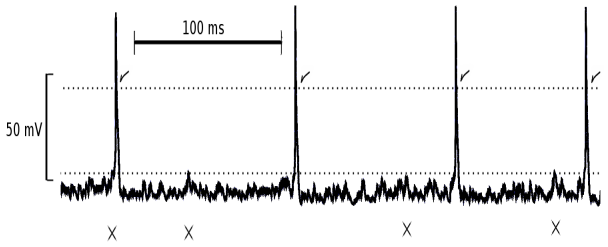

Figure 3.1: The horizontal lines show different thresholds that can be used to detect APs. The crosses mark times of where errors in detecting an AP with a low threshold.

3.1.1 Counting spikes using pulsed functions.

It is convenient to describe spike trains by means of time-dependent delta-functions defined as

$$\delta(t) \quad = \quad \begin{cases} 1 \text{ if } t = 0, \\ 0 \text{ otherwise} \end{cases} \tag{3.1}$$

Assume the spike times from a recording like the one shown in Fig. 3.1 were $t_0, t_1, ..., t_N$. Spike trains recorded from neurons behave like stochastic processes (Perkel et al., 1967a,b). In other words, a spike train can be regarded as a sequence of random variables $\{s_t : t = 0, \delta_t, 2\delta_t, ..., T\}$ whose elements are labeled by the recording times and such that $s_t = 1$ if there is a spike at time t and 0 otherwise. Since time is discrete in this case (*i.e.,* it is possible to label every time step and count them), the stochastic process defined by the spike train is discrete as well. The spike times can be used in combination with the delta function in (3.1) to write the spike train as a function of time

$$s_t \quad = \quad \sum_{i=0}^{N} \delta(t - t_i), . \tag{3.2}$$

The notation used in (3.2) is very useful because it provides with a framework for quantification of spike trains. For instance, it is now possible to write a formula for the number of spikes in the train within a time interval $[a, b]$:

$$C\left([a, b]\right) \quad = \quad \sum_{t \in [a,b]}^{N} s_t. \tag{3.3}$$

The probability of observing a spike in the interval $[a, b]$ can be approximated

by dividing the spike count from (3.3) by the length of the time interval:

$$R([a,b]) \;=\; \frac{C([a,b])}{b-a}. \tag{3.4}$$

Notice that to obtain R in units of pulses per second (pps) it would be necessary to multiply by 1000.

A spike train is called *stationary* if the probability of finding a spike in an interval of length T is the same regardless of the location in the recording and of the size of the interval T. In other words, the train is *stationary* if the neuron from which the train was recorded can be expected to fire, on average, the same number of action potentials within any two time-intervals of the same length. A consequence of stationarity is that if N is the average number of spikes in T ms, then $R(0,T) = N/T$ will converge to the true probability of spiking as T increases. Consequently, if a spike train is stationary, the count in (3.3) only depends on the length of the interval and $R(0,T)$ can be regarded as the average spike frequency in an interval of length T, provided T is long enough(see Fig. 3.2).

Now let τ be a random variable representing the waiting times between spikes, or *interspike intervals* from a spike train. Then, for the spike train $t_0, ..., t_N$, τ takes values $\tau_i = t_i - t_{i-1}$ for $i = 1, ..., N$. A count of the interspike intervals can be calculated using delta functions:

$$D(\tau) \;=\; \sum_{i=1}^{N} \delta\{\tau_i = \tau\} \tag{3.5}$$

A plot of D for each value of τ is the histogram of interspike intervals. The variability of interspike intervals is usually assessed by calculating the *coefficient of variation* of the interspike intervals, ν_τ, defined as the quotient between the mean and the standard deviation of the interspike intervals, $s_\tau/\bar{\tau}$.

The multiplicative inverses of the interspike intervals form a sequence $f_1 = 1/\tau_1, ..., f_N = 1/\tau_N$ called the *instantaneous firing rates*. To express the rates in units of pulses per second (pps), the instantaneous firing rate of the train can be obtained by multiplying each of the elements of the sequence $f_1, ..., f_N$ by 1000.

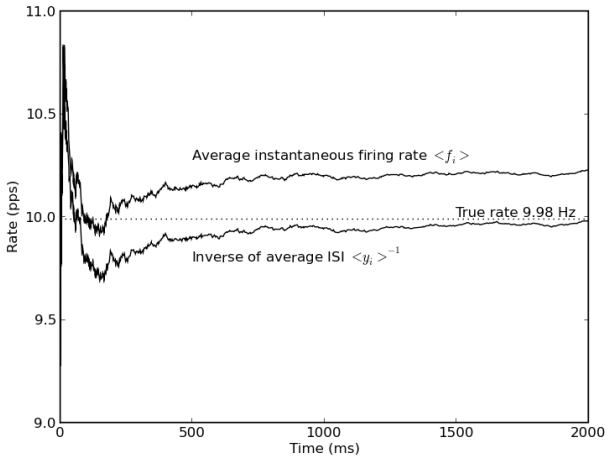

Figure 3.2: Comparison between calculations of rate. In this example the spike train had an average of 9.98 pulses per second. The solid lines show, respectively, the calculation of the average of all instantaneous firing rates, $\bar{f}$ (top) and the inverse of the average interspike interval, $1/\bar{\tau}$ (bottom), both calculated as functions of time. The dashed line illustrates the relative frequency of spiking obtained using (3.4).

The average firing frequency of the neuron can be approximated by calculating the multiplicative inverse of the average interspike interval, $1/\bar{\tau}$. It can be demonstrated assuming that spike trains are stochastic point processes that the inverse of the average interspike interval $1/\bar{\tau}$ converges to the true spiking rate for large enough T. Another approximation that is accurate only in a limited number of cases can be obtained by calculating the average of the instantaneous firing rates, $\bar{f}$. Note these two quantities are not the same. In fact, as shown in Fig. 3.2, $\bar{\tau}^{-1} \leq \bar{f}$.

3.2 Quantification of pairwise spiking activity.

The following paragraphs explain how to calculate correlation functions from a pair of spike trains and detect significant fluctuations indicative of correlated activity.

3.2.1 Correlation functions.

Now assume we have two spike trains recorded simultaneously. Let two spike trains be represented by the sequences $t_i^{(1)}$ and $t_j^{(2)}$, where $i = 1, ..., N_1$ and $j = 1, ..., N_2$. Without loss of generality, assume train 1 has less than or equal spikes than train 2. Train 1 will be referred to as the *reference* train and train 2 will be referred to as the *response* train. Following the notation introduced above, let the spike trains from two different neurons be represented by pulse functions, this time indexed

$s_1(t)$ and $s_2(t)$ for $n = 1, 2$. One way to assess if the two spike trains s_1 and s_2 are independent is to calculate their correlation function. In a continuous setting, correlation functions are just convolutions of two time dependent functions. In a discrete space like the time sample described here, the correlation function between two spike trains is written as

$$C_{1,2}(h) \quad = \quad \sum_{t=1}^{N_T} s_1(t) \cdot s_2(t+h). \tag{3.6}$$

where h is a *time difference* or *delay* between a spike in the response train and a spike in the reference train. The values for h are typically chosen to be within a relevant time scale for the phenomenon under study. For instance, in situations where nearly coincident spiking is studied, the typical interval for h is $[-100, 100]$ ms. The count is then repeated for different values of h, thus obtaining a function that depends on the time-delays between spikes from the two trains. This function is often called *cross-correlation* function if the two trains are different and *auto-correlation* function if the same train is used as response and as reference. Note that $C_{1,2}(h) = C_{2,1}(-h)$, so it is not necessary to do another calculation to obtain $C_{2,1}(h)$.

The correlation function (3.6) counts the number of spikes from neuron 2 that occur h units of time apart from a spike from neuron 1. In other words, the function $C_{1,2}$ counts the number of *joint spikes* between neurons 1 and 2 at different time delays (Fig. 1.1 and 3.3). The graph of a correlation function (3.6) as a function of the time-delay h is called is called *correlogram*. Such a graph is often called *cross-correlogram* if the two spike trains are different. Similarly, if the reference and response trains are the same then the graph is also called *auto-correlogram*.

3.2.2 Independence between spike trains.

If the spike trains s_1 and s_2 are stationary and $C_{1,2}$ is divided by the number of spikes in the reference neuron, the result can be used to approximate the probability that

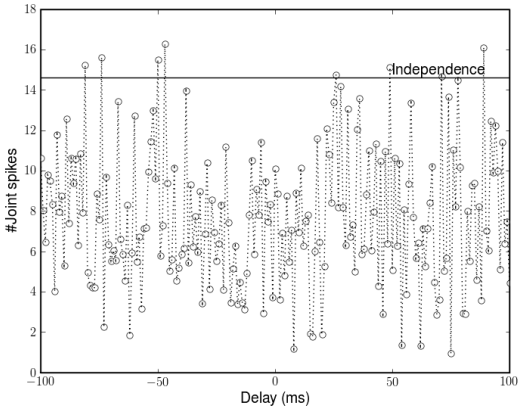

Figure 3.3: Correlogram between two independent spike trains. The horizontal line is the theoretical prediction for the delayed-spike counts that would result if the two spike trains were independent, which equals the expected number of spikes from the response cell.

spikes in train 2 occur at a delay of $t+h$ given a spike in train 1 occurred at time t

$$R_{1,2}(h) = \frac{C_{1,2}(h)}{C_2}. \tag{3.7}$$

$$\approx P\left[s_2(t+h)|s_1(t)\right]. \tag{3.8}$$

The two spike trains are independent if

$$P\left[s_2(t+h)|s_1(t)\right] = P\left[s_2(t+h)\right] \tag{3.9}$$

If $\bar{y}_2$ is the mean interspike interval of neuron 2, and the two spike trains are regarded as independent point processes, it can be shown rigorously that, the conditional probability that a spike from from neuron 2 occurs h time units apart from a spike in neuron 1 equals $1/\bar{y}_2$ Cox (1962); Perkel et al. (1967b)

3.3 Detection and quantification of significant fluctuations in correlation functions.

Large deflections in correlation functions may indicate a departure from independence in a pair of spike trains. The following two sections describe two methods for the detection of significant fluctuations in correlation functions. The two methods are applicable for any region of in the domain of a correlation function. The descriptions provided here are confined to peaks located in the central region around time-delay zero.

The first method is based on correcting the correlation function by subtracting a theoretical prediction of the correlation function that that would result if the

response train was independent from the reference train (see subsec. 3.3.1). The second method is a widely-adopted analysis technique (Keen and Fuglevand, 2004; Winges and Santello, 2004) in the field of motor control and it is based on finding a significant departure from an baseline count obtained outside an interval around the zero time-delay (see subsec. 3.3.2). The baseline count is in this case the average of the correlation function outside the time-delay interval $[-40, 40]$.

3.3.1 Peak detection using the correction for independence.

One way to quantify the level of dependence between two spike trains is to calculate a modified correlation function by subtracting the expected number of spikes in the response train that would occur if the two trains were independent Cox (1962):

$$\hat{C}_{1,2}(h) \quad = \quad C_{1,2}(h) - C_2. \tag{3.10}$$

The values of h at which the function is positive are the counts beyond what would result if the two spike trains were independent. Any peak around $h = 0$ can then be found by looking for a positive local maximum in $\hat{C}_{1,2}$ in a neighborhood of time-delay zero. Once found, the limits of the peak can be determined by simply looking for the closest values of h around the peak where $\hat{C}_{1,2}$ crosses zero, or, in other words, the closest values of h to the right and left from the peak at which the correlation function crosses the prediction for independence (solid, red line in Fig. 3.4A).

The significance of any value of $\hat{C}_{1,2}$ can be determined by using quantiles depending on the problem. It will be assumed in the rest of this document that any positive regions in the graph of $\hat{C}_{1,2}$ indicate the occurrence of nearly-coincident spikes.

3.3.2 Peak detection using Ellaway's cumulative sum.

A central cumulative sum Ellaway (1978) can be used to approximate the limits of a central peak. In brief, the mean of the counts outside a central region, usually the

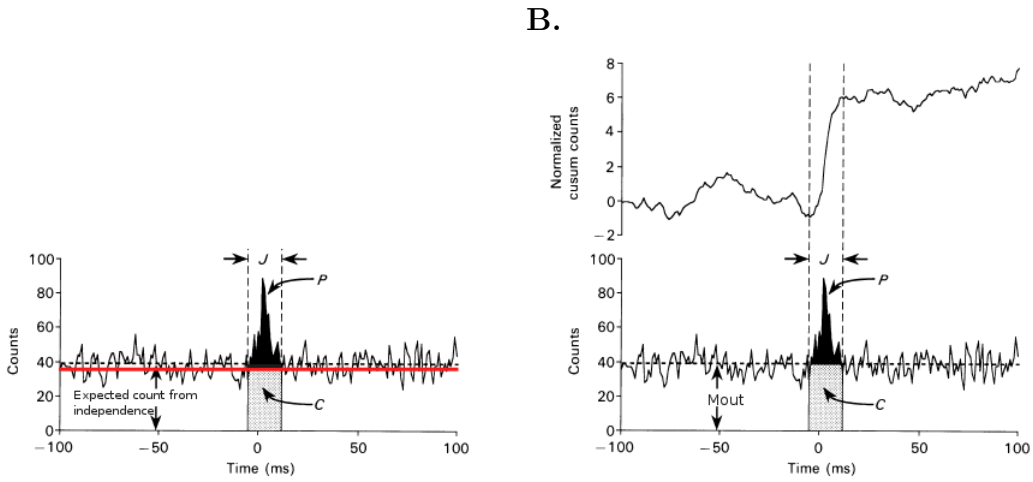

Figure 3.4: The outside mean M_{out} is shown as a dashed line in both plots for comparison. **A.** Peak detection using the correction for independence. The solid (red) line represents the predicted counts if the two spike trains were independent. **B.** Peak detection in correlograms using Ellaway's cumulative sum. From Nordstrom et al. (1992).

interval [-40,40], is calculated,

$$M_{out} = \frac{1}{120} \sum_{h \notin [-40,40]} C_{1,2}(h) \tag{3.11}$$

and used to approximate the average count that would result if the spike trains were independent. Then a cumulative sum of all the differences between the values of the correlation function and the outside mean M_{out} is determined by

$$\begin{aligned} S_M(h) &= \sum_{m=-100}^{h} (C_{1,2}(m) - M_{out}) \\ &= \sum_{m=-100}^{h} C_{1,2}(m) - (h - 100 + 1) M_{out} \end{aligned} \tag{3.12}$$

An increase in S_M near time 0 is used to delineate the central peak in the correlogram. The boundaries of the peak are defined as the values of h corresponding to 10 and 90% of the maximum S_M values (Schmied et al., 1993; Keen and Fuglevand, 2004). If there is a central peak, S_M is expected to be relatively flat outside the peak and to increase for h around the peak region (Fig. 3.4B). If S_M does not increasing significantly around zero, then the interval between -5 and 5 ms is used to delimit the peak region (Semmler and Nordstrom, 1995).

3.3.3 Indices to quantify the size of the peaks.

Note that in both methods described above, detection of the peak depends on finding a significant increase from a baseline count around the time-delay $h = 0$. In the independence-correction method, the baseline is the number of spikes in the response train C_2, whereas in the cumulative sum method, the base line is M_{out}.

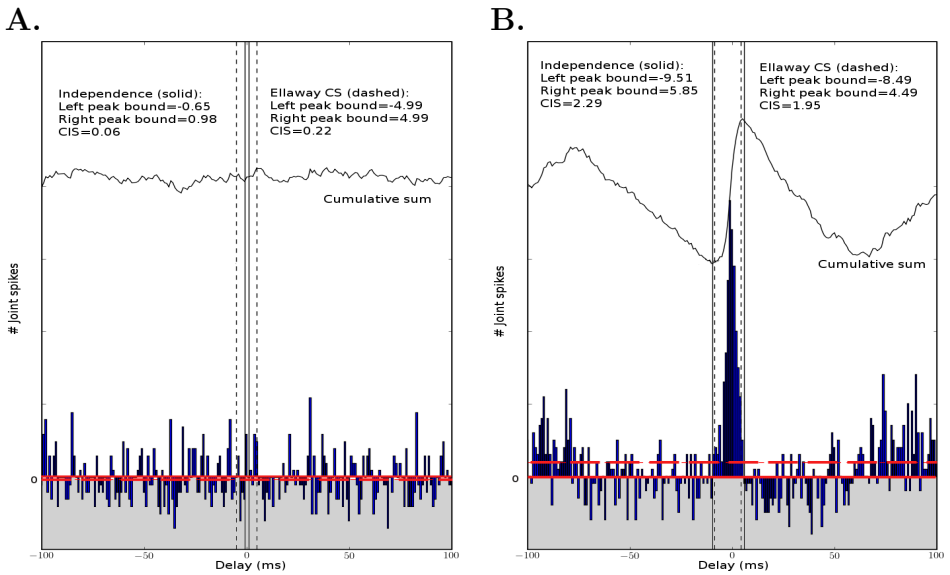

Figure 3.5: Peak detection from a correlogram count by using two methods and the calculation of the coincidence index CIS. Both plots show the correction using independence and the cumulative-sum method. The solid vertical lines are boundaries determined using the correction for independence, dashed vertical lines are boundaries determined by cumulative-sum method. The solid horizontal lines represent the base-line counts where $\hat{C}_{1,2} = 0$ using the correction for independence (the expected spike count in the response cell) and the dashed horizontal lines represent the baseline obtained by calculating the average count outside the central region, M_{out}. **A.** Example from a pair of spike trains with a very prominent peak around time-delay. **B.** Example from two spike trains for which the peak is not prominent.

To quantify the relative size of the peak with respect to the baseline, let P and C, respectively, be the regions of the peak above and below the baseline (Fig. 3.4). Two indices of coincidence widely used experimentally are calculated to quantify the size of the central peak. Both indices are quotients involving the total counts in regions P and C (Fig. 3.4). The first index will be called k equal to the index

k' used by Ellaway and Murthy (1985). In short, k is the ratio between the total number of spikes in the peak divided by the spike count from region C minus 1. The second index, referred to as common input strength, CIS (Nordstrom et al. (1992)), is the number of spikes in the peak after substracting the control spikes from region C, divided by the total time of the recording. Note CIS is in units of pps and can be regarded as the average rate of nearly coincident spiking observed from two spike trains.

Two examples of the calculation of the index CIS are shown in Fig. 3.5. The boundaries for the peak and the baseline counts are shown by vertical and horizontal lines, respectively. Fig. 3.5 also shows a comparison between the indices when calculated using the theoretical prediction for independent counts and when using the cumulative sum. The two methods agree in the case where the correlogram has a very clear peak (Fig. 3.5A). The error introduced by the approximations used in cumulative sum method when the peak in the correlogram is not clear are shown in Fig. 3.5B.

3.4 Overview.

The methods described in this chapter will be used in chapters 4 and 5 to analyze spike trains from spiking models of MNs.

Chapter 4

Models of spiking activity in neurons

4.1 Introduction

Every model of a natural phenomenon involves a compromise between the level of detail, mathematical tractability, and the computational cost of the numerical simulations of the model. This chapter provides a general overview of various approaches to modeling the dynamics of spiking activity in nerve cells. The different modeling approaches described in the first sections of this chapter will be used in chapter 5 to construct a model of simultaneous activity in spinal motor neurons that links spiking activity to different schemes of synaptic organization in the supraspinal inputs to MNs. Results from simulations aimed to answer specific questions about the relationship between nearly coincident spiking and different schemes of common synaptic input will be presented in chapter 5.

4.2 Excitability and modeling of spiking activity.

Excitable cells often display large, pulsed oscillations in their membrane potential called *spikes* or *action potentials* (APs). Each spike can be thought of as one event in a sequence of biophysical processes that occur within the cell which, in turn, may depend on the activity of other cells. Spikes, in turn, trigger different responses within their cells of origin as well as in other cells.

The physiological state of the membrane in an excitable cell can be described by a dynamical system. That is, a collection of variables linked in their time evolution. The system may be *deterministic*, or *stochastic*, meaning, respectively, that the relationships between the variables remain fixed from the outset, or change according to a probability distribution.

The model of choice will restrict the investigation and the interpretation of the results in different ways. For instance, the model can be biophysical, meaning that every expression in the model can be linked to a biophysical process (Hodgkin and Huxley, 1952; Morris and Lecar, 1981; Endresen et al., 2000; Herrera-Valdez and Lega, 2008a). Alternatively, equations could provide a phenomenological description that facilitates the mathematical analysis of the model at the expense of biophysical relevance (Fitz-Hugh, 1961; Izhikevich, 2003). In general the computational efficiency of a model will increase at the expense of explicit biophysical representation.

Sect. 4.3 reviews two methods for modeling spiking activity taking a stochastic approach following the approach taken by Perkel et al. (1967a), and Heeger (2000). Sect. 4.4 provides a general overview of dynamical systems theory and modeling of cellular excitability. A model of simultaneous spiking activity in MNs in response to common excitatory synaptic drive will be constructed using the concepts drawn from secs. 4.3-4.4

4.3 Spike trains as realizations of stochastic processes

Spike trains *in vivo* display a great deal of variability. The spike times of a neuron can be regarded as the realization of a stochastic process that follows certain rules. In principle, the randomness of the process may depend on factors like the firing rate of a neuron and the occurrence of previous spikes. The paragraphs below describe two simple but powerful ways to simulate the spiking activity of neurons using assumptions about the randomness in the spike times.

4.3.1 Spike trains as Poisson processes

A simple but very illustrative way to construct spike trains is based on the following assumptions:

P1. Spikes are sampled during a time interval $(0, t)$ with a time step δ_t small enough so that only one spike can occur within δ_t units of time. Time is assumed to

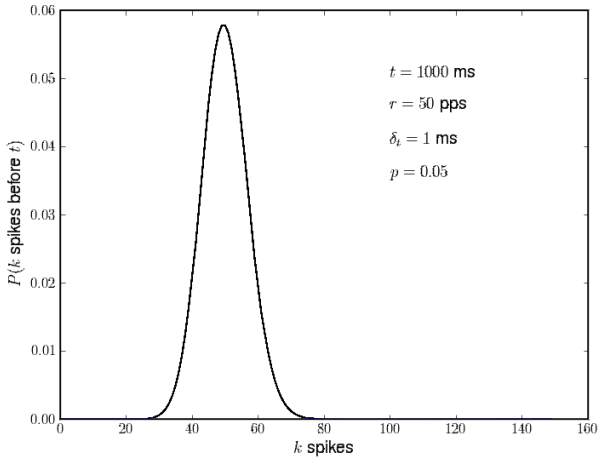

Figure 4.1: Poisson spike count.

be in milliseconds. The number of sample points n is then $[t/\delta_t]$ (the integer part of $t\ \delta_t$).

P2. The firing rate is almost constant within a time step. Note then that the probability that a spike occurs within δ_t seconds is $p \approx r\delta_t$.

P3. Spikes occur independently in non-overlapping intervals of length δ_t.

Sampling can then be thought of as a sequence of independent but identical Bernoulli trials in which the probability that a spike occurs is $p = r\delta_t$ (like tossing a coin at each time step to determine if a spike occurred or not). In consequence, the number of spikes in the interval $(0, t)$ behaves like as a binomial random variable with n trials, each having a probability of success p. An approximation to the probability of having k spikes before t milliseconds can be calculated explicitly in terms of the firing rate and the sampling interval using the binomial formula:

$$P\left(k \text{ spikes before } T\right) \approx \binom{n}{k} p^k (1-p)^{n-k}, \tag{4.1}$$

$$= \binom{n}{k} \left(r\delta_t\right)^k \left(1 - r\delta_t\right)^{n-k}, \tag{4.2}$$

$$= \binom{n}{k} \left(\frac{rt}{n}\right)^k \left(1 - \frac{rt}{n}\right)^{n-k}. \tag{4.3}$$

An exact expression for the probability that k spikes occur before T can then be obtained by letting the number of subintervals n increase to infinity in Eqn. (4.1)

to obtain

$$P\left(k \text{ spikes before } T\right) \;=\; \frac{(rt)^k}{k!} exp\left(-rt\right), \tag{4.4}$$

which has the form of a Poisson probability density function (see Fig. 4.1 and appendix 4.6 for the calculation). In other words, the spike count constructed using assumptions P1-P3 is a *Poisson random variable*.

Poisson processes in which the firing rate r is constant are called *homogeneous*. It is possible to construct *non-homogeneous* Poisson processes using the same hypotheses as above as long as r remains almost constant in the subintervals determined by δ_t.

Following the notation used in previous sections, let τ represent the waiting time between any two spikes. There are two statistics of interspike intervals that are widely used in neurophysiology to quantify the variability in spike trains. The first statistic is called the *Fano factor* and is defined as the variance divided by the mean, $F_\tau = \sigma_\tau^2/\mu_\tau$. The second quantity, created from the Fano factor is called the *coefficient of variation*, ν_τ, equal to the ratio between the standard deviation and the mean. That is, $F_\tau = \sigma_\tau \nu_\tau$. It can be shown using Eqn. (4.4), that the mean and variance of the spike count in an interval $(0, t)$ are both equal to rt. That is, the Fano factor is always 1 in a Poisson process. The converse is not necessarily true; i.e. if the mean and standard deviation of a stochastic process are the same it does not follow that the stochastic process is Poisson.

Interspike intervals from a Poisson spike train. The distribution of interspike intervals from a Poisson spike train is readily obtained by using Eqn. (4.4). The probability that no spikes occur before a time t can be found by letting $k = 0$ in Eqn. (4.4):

$$P(\text{no spike before } t) \;=\; exp(-rt). \tag{4.5}$$

The probability of observing a spike any time before t ms have passed is

$$P(\text{spike before } t) \;=\; 1 - exp(-rt). \tag{4.6}$$

The expression (4.6) gives the *probability distribution function* for the waiting times in a Poisson process. Since the Poisson process in this case is the spike count, (4.6) represents the distribution function for the interspike intervals in a train with rate r. The expression in (4.6) indicates that the likelihood of not observing a spike before τ is exponentially smaller as τ increases. The probability that an interspike interval is exactly τ can be obtained by differentiating the distribution function (4.6)

$$\begin{aligned} \frac{dP}{dt} &= \frac{d}{dt}\left[1 - exp(-r\tau)\right] \\ &= r \cdot exp(-r\tau). \end{aligned} \tag{4.7}$$

Equation (4.7) gives the *probability density function* of τ, and indicates that the interspike intervals from a Poisson spike train are exponentially distributed ((see Fig. 4.2)B). It can be shown using (4.7) that the mean and standard deviation of the interspike intervals from a Poisson spike train are both equal to $1/r$. That is, the coefficient of variation of the interspike intervals obtained from a Poisson spike train equals 1.

Generating Poisson spike trains numerically. In view of (4.7), the simplest way to generate a Poisson process is to generate a sample of interspike intervals $u_1, ..., u_N$ from an exponential distribution and reconstruct the spike train by successively adding the intervals to a first spike time t_0 (which could be zero). The first spike time would be $t_1 = t_0 + u_1$, the second time would be $t_2 = t_0 + u_1 + u_2$, and so on until $t_n = t_0 + u_1 + ... + u_n$.

If a sample generator for exponential distributions is not available, a Poisson spike train can be generated by an iteration process. Recall that the probability that one spike occurs at time t is $p(t) = r(t) \cdot \delta_t$. Note $p(t)$ is not necessarily constant. For each time step, choose a random number a between 0 and 1. If $a < p(t)$, then a spike is generated at this time (Fig. 4.2A). The resulting exponential distribution of the interspike intervals characteristic of Poisson spike trains is shown in Fig. 4.2B.

After the occurrence of a spike in a real neuron there is an absolute refractory period during which no more spikes can occur. This means that a neuron cannot have arbitrarily small interspike intervals. Instead, the smallest intervals must be

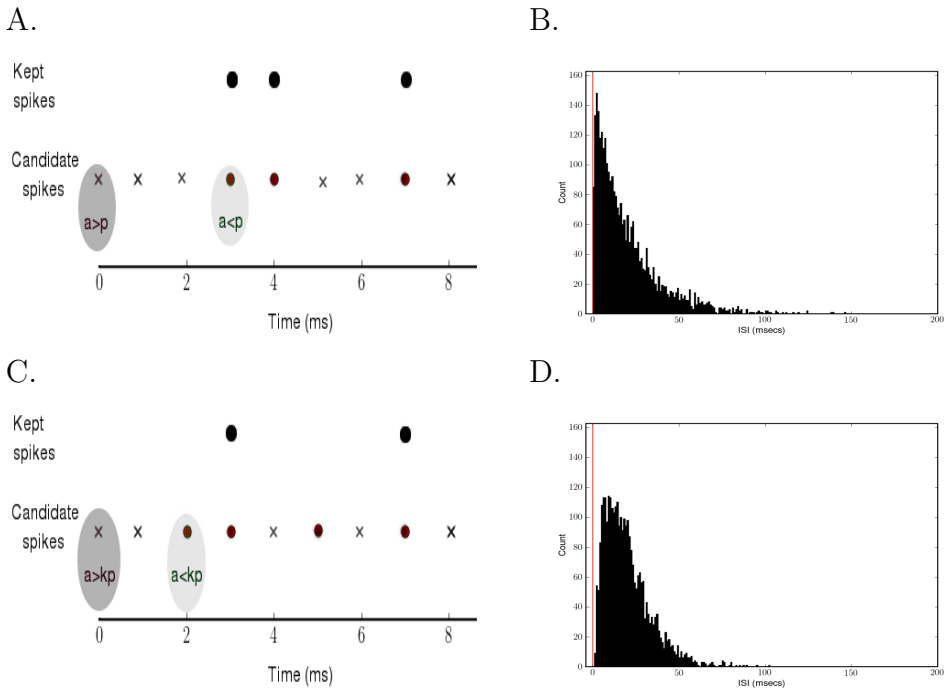

Figure 4.2: Spike trains as realizations of stochastic processes. A. Poisson process. B. Interspike interval histogram from a Poisson train. C. Renewal process. D. Interspike interval histogram from a train generated using a renewal process. The red line indicates the zero interspike interval. Both examples of spike trains were generated with $r = 50$ pps, $\delta = 1$ ms, and a total time of 100 s. The renewal spike train was generated using a refractory period $\rho = 2$ ms.

at least as long as the absolute refractory period. In cases where this consideration is crucial, it is no longer suitable to use Poisson processes to describe the spiking of a neuron. The following paragraphs describe a modeling approach that accounts for refractory periods by shaping the randomness of the process with an the extra requirement of a minimum waiting time between spikes.

4.3.2 Spike trains as renewal processes

The Poisson model described in the previous section can be modified to incorporate the existence of an absolute refractory period. As with the Poisson process, there are at least two ways to do this.

To generate the spike trains with refractory periods using an iteration process,

it is necessary to modify the assumption about independent spiking from the construction of the Poisson spike train so that spike generation now depends on the occurence of the last spike. Stochastic processes with this characteristic are called *renewal processes*. First, an integer k representing the renewal time that corresponds to the refractory period is found by setting $k = [\rho/\delta]$. A process similar to that used for the Poisson trains is carried out by generating a random number a between 0 and 1 at each time step. If $a < k \cdot p(t)$, then t is a candidate spike time (Fig. 4.2C). Note the number of candidate spike times found this way is k-times larger than it would be in a Poisson process since the integer k increases the chance that a produces a candidate time. The spike train is determined by keeping only every kth candidate spike time. For instance, if the refractory period is $\rho = 2$ ms, then the expected number of candidate spike times is twice as many as in a Poisson train with the same rate and sample step. However, keeping every second spike results, on average, in a number of spikes that corresponds to the desired firing rate.

The probability density function for the interspike intervals obtained from the train generated as a renewal process is described by a gamma function with parameters k and r:

$$\begin{aligned} p(\tau;\alpha,r) &= \frac{r^k \tau^{k-1}}{(k-1)!} exp(-r\tau) \\ &= \gamma(\tau;k,r). \end{aligned} \tag{4.8}$$

Gamma functions with $k > 1$ have a slower rise to peak in comparison to when $k = 1$ (Fig. 4.3). The particular case $k = 1$ is an exponential function $\gamma(\tau;1,r) = rexp(-r\tau)$, which has exactly the same functional form as (4.7), the probability density function for the interspike intervals from a Poisson train. Indeed, the iteration process just described to obtain spike trains with a refractory period is the same as for the Poisson trains if $k = 1$.

Hence, another way to generate spike trains with refractory periods is to generalize the density function for the interspike intervals originally derived from the Poisson train and use gamma functions. Therefore, a spike train with a refractory period can be generated by adding intervals sampled from a gamma distribution as

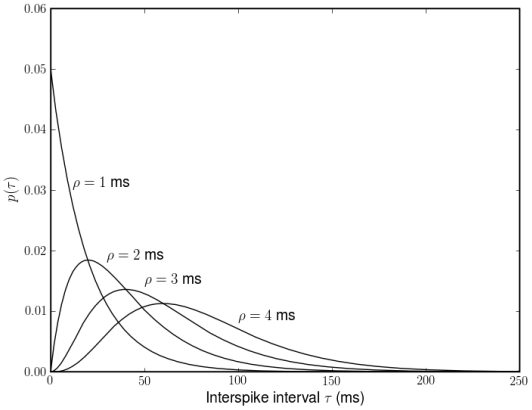

Figure 4.3: Probability density functions of interspike intervals from renewal spike trains with refractory periods $\rho = 1, 2, 3$, and 4 ms.

explained above for Poisson trains.

The mean of the interspike interval in renewal trains is the same as for the Poisson process ($\mu_\tau = 1/r$). However, the variance of the gamma-interspike intervals is $1/rk$. In consequence, if τ has a gamma distribution, then $F_\tau = 1/k$ and $\nu_\tau = 1/\sqrt{k}$. For instance, if the refractory period is 2 milliseconds, then the coefficient of variation of the input trains is $\nu_\tau \approx 0.7$.

It is widely believed that cortical interspike intervals have coefficients of variation close to 1. This belief has been widely used in the literature to justify stochastic modeling of cortical spike trains using Poisson processes. However interspike interval distributions of cortical cells are highly variable (Softky and Koch, 1993). The coefficients of variation obtained from interspike intervals recorded in many cortical areas range between 0.4 to 1.2 with a mean around 0.8, which corresponds well to the theoretical prediction obtained from a gamma distribution with a refractory period of 2 ms. In addition, the distributions of interspike intervals in cortical cells have shapes that agree more with the profile of gamma distributions.

The following section describes a deterministic approach to modeling spike trains.

4.4 Spike trains as events in a deterministic dynamical system

The membrane dynamics of an excitable cell can be modeled with a dynamical system written in generic form as a system of ordinary differential equations

$$\frac{dv}{dt} = f(v, w, x), \tag{4.9}$$

$$\frac{dw}{dt} = g(v, w, x), \tag{4.10}$$

$$\frac{dx}{dt} = \varepsilon h(v, w, x), \tag{4.11}$$

where the variable v represents the *membrane potential*, w is a *recovery variable*, and x is an *adaptation variable* typically slower than v and w. The functions f, g and h are assumed to have no explicit dependence on time (Av-Ron et al., 1993). The system (4.9)-(4.11) is called biophysical if every variable or process can be associated with a biophysical mechanism (Hodgkin and Huxley, 1952; Morris and Lecar, 1981; Endresen et al., 2000; Herrera-Valdez and Lega, 2008b). Spikes can be extracted from the dynamics of v by recording the times at which v crosses a predetermined threshold, selected to minimize the probability of erroneous detection of action potentials (Fig. 3.1).

The parameter ε controls the rate of change of x. If ε is sufficiently small, it can be assumed that $dx/dt = 0$, so x becomes a constant parameter (hence no longer a dynamical variable) thereby reducing the system to two equations (4.12)-(4.13). The remaining equations are called the *fast subsystem* since they include the two faster variables from the original system. One instance in which such a reduction is reasonable can be found in biophysical systems intended to model cellular excitability in which spike frequency adaptation or bursting are not relevant behaviors. Note, however, that it is possible to artificially obtain bursting and spike frequency adaptation from phenomenological models using only two equations (Izhikevich, 2004).

The following sections contain an overview of biophysical systems (subsec. 4.4.1), followed by a minimal review of concepts from dynamical systems theory (subsec. 4.4.2), and a survey of phenomenological systems (subsec. 4.4.3) to point out that phase plane analysis and bifurcation theory can be used to construct phenomeno-

logical systems with the same qualitative behavior as biophysical systems.

4.4.1 Overview of Biophysical models

Biophysical models of membrane excitability are such that f and g from (4.9)-(4.11) are explicitly written in terms of the membrane capacitance, rate of change in membrane potential, and the different ion fluxes mediated by membrane proteins. For instance, a basic biophysical system that can be used to reproduce all the electrophysiological properties of MNs mentioned in subsect. 2.1 can be written as

$$C_m \frac{dv}{dt} = I - I_{ion}(v, w, x) \tag{4.12}$$

$$\frac{dw}{dt} = \frac{w_\infty(v) - w}{\tau_w(v)} \tag{4.13}$$

$$\frac{dx}{dt} = \varepsilon\left(-I_{Ca} - r_x x\right) \tag{4.14}$$

where C_m is the membrane capacitance ($\mu F/cm^2$), I is a parameter representing external current injection from an electrode. All currents are in units of (nA/cm^2). Since under current injection MNs display spike-frequency adaptation and *burst-like* behaviors in the form of doublets, triplets or more spikes, it is necessary to have a third, slower *adaptation* variable x in the model. It has been demonstrated in neurons and pancreatic cells that one biophysical mechanism underlying adaptation and bursting involves a change in the total potassium conductance that depends on slow dynamics of the calcium concentration beneath the membrane. To include this in the model, x is assumed to be the calcium concentration beneath the membrane, with a parameter ε controlling the rate at which $[Ca]_i$ increases as a function of the total Ca^{2+}-current I_{Ca}, and r_x represents the removal rate of Ca^{2+}. The parameter ε is inversely proportional to the product of Faraday's constant ($F = 96.649 C/mM$) times the volume of the cell, so that εI_{Ca} is in units of concentration per unit time.

The adaptation variable $x = [Ca]_i$ is necessary for the model to display behaviors like spike frequency adaptation and the initial "burst-like" behavior of MNs in response of current stimuli of large amplitudes. There are several physiological

mechanisms that can give rise to burst-like behaviors. One typical example in which bursting occurs is when the total conductance for K^+ changes depending on a slow increase in the submembrane Ca^{2+}-concentration. The parameter r_x primarily affects the interval between sustained spiking episodes whereas ε primarily affects the duration of repetitive spiking.

Existing experimental evidence indicates that the MNs modeled in this dissertation only display burst-like spiking (in doublets or triplets) and spike frequency adaptation in response to current injection but these behaviors are not commonly observed in the intact animal. Therefore, the biophysical systems used in this dissertation to model MNs will be two-dimensional and will not include adaptation variables (*i.e.*, $dx/dt = 0$).

The term $I_{ion}(v, w, x)$ in (4.12) represents the total ionic current and equals the sum of currents mediated by ion channels and transporters. The expressions for the membrane currents and the gating variable w depend on the assumptions used to construct the system.

The biophysical models used here were originally used by Hodgkin and Huxley (1952) to describe the dynamics of membrane potential in the squid giant axon. Such models assume that the cell membrane is an electrical circuit where the lipid bilayer is represented by a capacitor and membrane spanning proteins that mediate ion flux are resistors arranged in parallel. In this case all the currents are expressed as products of a conductance times a difference between the membrane potential and a reversal potential that depends on the ion(s) permeable through the channels.

4.4.2 Overview of dynamical systems theory.

A brief review of concepts from the theory of dynamical systems is presented within the scope of 2D-systems of the form (4.9)-(4.10).

The state of membrane is described at any point in time by the $(w(t), v(t))$. For instance, if a cell is represented by the biophysical system (4.12)-(4.13) then the electrophysiological behavior of the cell is assumed to be described by its membrane potential and the probability of opening of its K^+ channels. The two-dimensional

(2D) space where the states of the system "live" is called *phase space*, or in this case, *phase plane* because there are only two variables in the system. The trajectory described by the time evolution of the system from a starting point (w, v) is called the *orbit* of (w, v) and can be represented graphically as a curve in the phase plane. A graphical representation of the orbits of the system for a particular choice of parameters is called a *phase portrait*. Different parameter choices may change the phase portrait, possibly implying global qualitative changes in the time-evolution of the system.

The concepts discussed in the rest of this section will be illustrated with examples extracted from a 2D-biophysical system of the form

$$C_m \frac{dv}{dt} = I - I_{ion}(v, w, x), \tag{4.15}$$

$$\frac{dw}{dt} = \frac{w_\infty(v) - w}{\tau_w}, \tag{4.16}$$

with

$$\begin{aligned} I_{ion} &= I_{Na} + I_K + I_L \\ &= g_{Na} m_\infty^{l_m}(v)(v - v_{Na}) + g_K w^{l_w}(v - v_K) + g_L(v - v_L), \end{aligned} \tag{4.17}$$

and

$$p_\infty = \left[1 + exp\left(-a_w(v - v_w)\right)\right]^{-1}, \; p \in \{m, w\}, \tag{4.18}$$

where I represents the amplitude of an externally applied current, g_{Na}, g_K, g_L, the specific Na^+-, K^+-, and leak conductances in mS/cm^2, p_∞ is the steady state proportion of open K channels, a_w controls the slope of the steady state opening of K-channels (mV^{-1}) and the time constant of K activation τ_w in ms^{-1}. The steady Different choices of the parameters $g_{Na}, g_K, g_L, v_{Na}, v_K, v_L, v_m, v_w, a_m$ and a_w were made to demonstrate how the behavior of the system can be modified and predicted using a geometrical analysis of the equations.

An initial set of definitions will be presented and illustrated with a model using a set of parameters that turns the system into a pacemaker that displays periodic

spiking. These first definitions will be illustrated with Figs.Fig. 4.4-4.6. The concepts of bistability and bifurcation will be defined and illustrated with Figs. 4.6-4.7 by choosing parameters that change the behavior of the system.

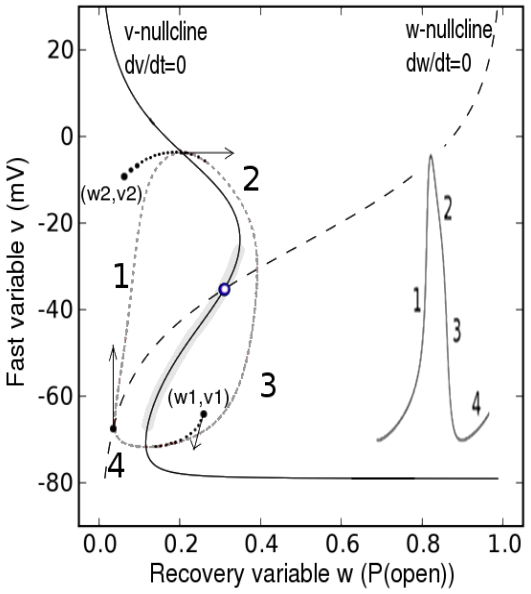

Figure 4.4: General phase portrait of dynamical system (4.15)-(4.18). The parameters were such that the system displays sustained spiking. The system has a unique, unstable fixed point and a globally stable limit cycle shown as a closed dotted curve (red). All trajectories starting near the fixed point are repelled by it and converge to the limit cycle (orbit starting at (w_1, v_1)). Likewise, orbits starting outside the limit cycle eventually converge to it (orbit starting at (w_2, v_2)). In fact, if the parameters of the system are such that the fixed point is unique and located in the shaded region and the angles between the nullclines are similar, then there will be a globally stable limit cycle. The inset shows an action potential. The numbers label different stages of the action potential and their corresponding portions within the limit cycle. Modified from Herrera-Valdez and Lega (2008b).

A phase portrait for the model (4.15)-(4.18) in a case where self-sustained action potentials occur is shown in Fig. 4.4. The inset in the figure shows the time course of an action potential with different phases. The closed curve in dots illustrates the orbit described by the spikes. Note that time is not represented in the phase plane. Since neither f nor g depend explicitly on t, the evolution of the system from any initial condition does not depend on the starting time. This kind of system is called *autonomous*. The tangent to an orbit passing through any point (w, v) has a unique slope $dv/dw = f(v, w)/g(v, w)$ provided $g(v, w) \neq 0$. The trajectories of the system can then be unambiguously determined without solving the system by simply evaluating f and g at different points in the phase plane. An arrow can be placed at any (w, v) pointing in the direction determined by the signs of f and g.

For instance, if $f(v, w) < 0$ and $g(v, w) > 0$, then both v and w decrease ($dv/dt < 0$ and $dw/dt > 0$) at the point (w, v), and the arrow should point down and to the left (Fig. 4.4 point (w_1, v_1)). A flow chart of the trajectories can be constructed this way by placing arrows over the phase plane.

Nullclines and fixed points. Characterizing the behavior of the system depends on finding transitions at which the variables switch from increasing to decreasing and viceversa. These transitions occur at points where the time-derivative of v and w is zero. The conditions $dv/dt = 0$ and $dw/dt = 0$ are satisfied by sets of points in the phase plane that form curves called respectively, the v- and w-*nullclines* (Fig. 4.4). Note then that a nullcline is a set of points for which one of the variables of the system stays constant; i.e. its time derivative is zero. For instance, in the system (4.12)-(4.13) the v-nullcline is a curve containing points at which $dv/dt = 0$ (Fig. 4.4 solid line). Similarly, the w-nullcline is a curve formed by points where $dw/dt = 0$ (Fig. 4.4 dashed line). As a consequence, the system evolves in the direction of w at any point in the v-nullcline. Analogously, the system evolves in the direction of v along the w-nullcline. This behavior can be found at states that correspond to turning points in action potentials, where the trajectory intersects the v-nullcline at the maximum and minimum values of v. For instance, at the peak of the action potential, $dv/dt = 0$ but $dw/dt > 0$, meaning that the membrane potential is not changing while the proportion of open potassium channels increases (illustrated by an arrow in Fig. 4.4 at the top of the loop).

When expressed as functions of v, the typical shapes of the v- and w-nullclines in biophysical systems are, respectively, cubic and sigmoidal. The points where the nullclines intersect are called *fixed points*. By definition, the system does not change at fixed points since the nullclines intersect when $dv/dt = 0$ and $dw/dt = 0$. In consequence, orbits starting at fixed points consist of only one point. The fact that the system is autonomous guarantees that except for fixed points, every other point in the phase plane is part of an orbit and no two orbits pass through the same point.

Local and global stability. A fixed point is *locally stable* if it attracts nearby trajectories. For instance, the fixed point shown as a solid dot in Fig. 4.5 is locally stable. This means that if the system is slightly perturbed and moved away from a locally stable fixed point, the trajectory from the perturbation will go back to the fixed point. For instance, the membrane potential of many neurons usually tends to return to rest after small perturbations caused by synaptic noise or oscillations in the local field potential surrounding a neuron. If a fixed point attracts arbitrarily distant trajectories it is called *globally stable* (Fig. 4.6).

Alternatively, fixed points that repel nearby orbits are called *unstable*. As already pointed out, the orbit of an unstable fixed point consists of one point. The fixed point shown as an open dot in Figs. 4.4 and 4.6B is unstable. Interestingly, locally stable and unstable fixed points can coexist. In other words, it is possible to select the parameters of the system so that it has more than one fixed point (Fig. 4.7).

Attractors. The local and global stability of fixed points can be used to find regions in phase space called *attractors* because nearby and possibly distant orbits converge toward them. For instance, many neurons have a resting membrane potential toward which they come back after the occurrence of a spike. In this case the system goes back to a single point in the phase space. This kind of attractor is a stable fixed point.

There is another kind of attractor called *limit cycle*. For instance, pacemaker cells display sustained periodic spiking as in Fig. 4.4 and 4.5. In this case the system is trapped into a loop that describes the trajectory of the pacemaker oscillations in phase space. *Limit cycles* typically exist around fixed points.

As with fixed points, limit cycles can be locally or globally stable. The pacemaker oscillations in Fig. 4.4 are globally stable limit cycles around a locally unstable fixed point. A *basin of attraction* is defined as the set of the states whose orbit eventually gets trapped into an attractor. An attractor is globally stable if its basin of attraction is the entire phase space. Systems with only one attractor are called *monostable*. For instance, the basin of attraction for the limit cycle in Fig. 4.4 is

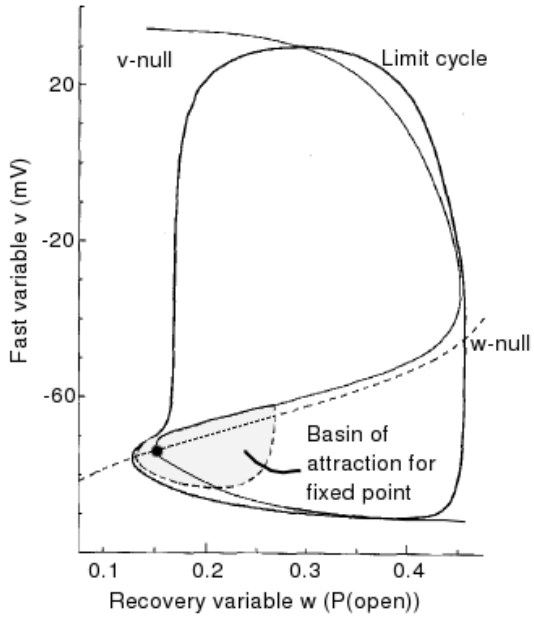

Figure 4.5: Phase portrait of 4.15)-(4.16) near a subcritical Andronov-Hopf bifurcation. The shaded region represents the basin of attaction of the fixed point. The system is bistable, with a locally stable fixed point and a locally stable limit cycle shown as a closed curve. All trajectories starting within the shaded region will go back to the resting point and trajectories starting outside the shaded region converge to the limit cycle. The closed curve describes the evolution of the system as periodic action potentials occur in response to a brief pulse of current injection that takes the state of the membrane into the basin of attraction of the limit cycle. Modified from Av-Ron et al. (1993). Parameters: $l_m = 3, l_w = 4$, $g_{Na} = 120$, $g_K = 36$ and $g_L = 0.3$ all in mS/cm^2; $v_{Na} = 55$, $v_K = -72$, $v_L = -50$, $v_m = -31$ and $v_w = -46$ all in mV; $a_m = 0.065$, $a_w = 0.055$, $r = 0.04$ ms^{-1},$C_m = 1$ nF/cm^2 and $I = 0$. Example from Av-Ron et al. (1993)

the whole phase plane. The convergence of trajectories toward the limit cycle are shown by two orbits starting at points inside and outside the limit cycle. Similarly, the basin of attraction for both of the fixed points shown in Fig. 4.6A and C is again the entire (w, v)-plane.

If the basin of attraction is only a subset of the phase space then the attractor is locally stable. The example shown in Fig. 4.5 is such that a locally stable fixed point coexist with locally stable limit cycle. The basin of attraction of a locally stable fixed point is shown by a shaded area. The rest of the phase plane is the basin of attraction for the limit cycle. This is an example where the system has more than one attractor, in which case the system is called *bistable*.

Bifurcations. It is important to notice that if the parameters of the system change, then the local shape and location of the nullclines will change, potentially affecting the existence and stability of the fixed points (Fig. 4.6).

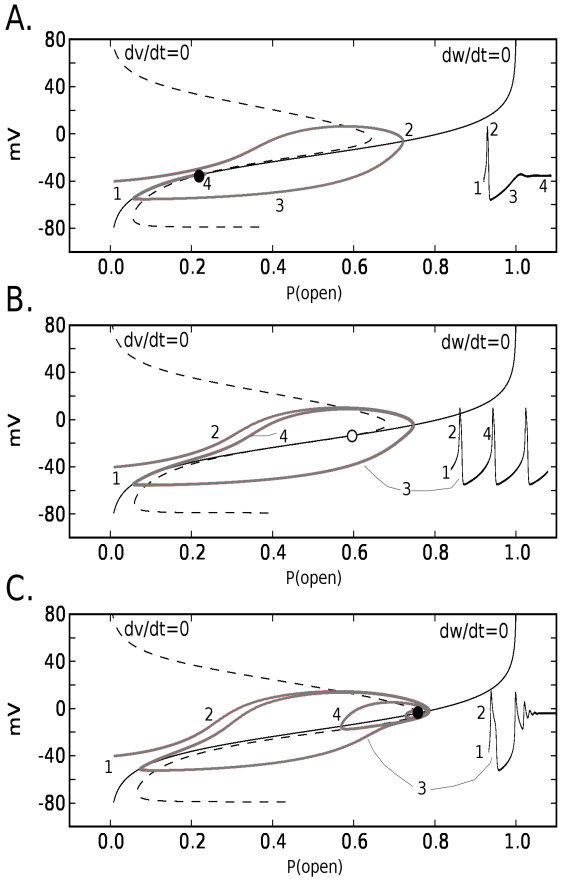

Figure 4.6: Convergence of the system (4.15)-(4.18) to globally stable attractors. The evolution of the system as spikes takes place starting from a starting initial condition labeled "1" is illustrated in each of the phase planes. The insets illustrate the corresponding time course of the membrane potential. The parameter g_{Na} was increased resulting in different v-nullclines and a unique fixed point in each case. The location and stability of the fixed point were different for different values of g_{Na}. **A** and **C** show examples where the fixed point is globally stable. Note the convergence of the trajectories to the fixed point both cases. **B.** Unstable fixed point with a globally stable limit cycle. The system displays sustained spiking behavior as also shown in Fig. 4.4. Note the convergence of the system into the limit cycle. Example from (Herrera-Valdez and Lega, 2008a).

A dynamical system is said to undergo a *bifurcation* if the stability or the number of fixed points changes for different values of a parameter. The parameter is called *bifurcation parameter* and the values at which bifurcations occur are called *bifurcation values*.

Figure 4.6 shows three examples where the parameter g_{Na} is increased resulting in different v-nullclines, always with a unique fixed point, and such that the location and stability of the fixed point changes. The fixed point is globally stable for lower values of g_{Na} (Fig. 4.6A) but becomes unstable as it moves along the the middle portion of the v-nullcline (Fig. 4.6B). The phase portrait of the system for a choice

of parameters where the system has an unstable fixed point is shown in Fig. 4.6B. In this case the system has a globally stable limit cycle (the system displays periodic oscillations). The fixed point becomes stable again as g_{Na} is further increased (Fig. 4.6C). The location at which the fixed point becomes stable again is near the turning point of the v-nullcline. In the absence of no other changes in parameters, the system would cease to spike as soon as the fixed point becomes stable. The sytem would only respond with a spike only when the state of the cell is perturbed sufficiently, as it would be the case when the membrane potential is depolarized under a large pulse of current injection. Regardless, the membrane returns to the resting state as soon as the spike is over. The highly depolarized resting state shown in Fig. 4.6C is an example of a phenomenon called *depolarization block* which can be thought of as a pathological depolarized state of the cell. This is an example of a *supercritical Andronov-Hopf* bifurcation.

There are several kinds of bifurcations but only four of them are needed to classify the behavior of excitable cells. Fig. 4.7A shows an example of a bistable system near a bifurcation called *saddle-node* characterized by the loss of stability of a fixed point as it merges with an unstable fixed point and they both eventually dissapear. In this case, the bifurcation is demonstrated by increasing the value of the current parameter I. In fact, the two fixed points merge and then dissappear. This happens because the increase in the injected current causes the v-nullcline to shift toward larger values of w, eventually bringing the two fixed points located at lower v-values closer together. The two merged fixed points dissappear as the injected current is further increased. Fig 4.7B shows a *bifurcation diagram* for I.

The behavior of the system at the bifurcation from single spiking to sustained firing defines the *excitability* of the cell. There are two classes of excitable cells. Class I cells are such that their initial frequency of sustained firing can be arbitrarily small. That is, their current-frequency relationship is continuous. Class II cells cannot have an arbitrarily slow firing frequency during sustained spiking. In other words, their current-firing frequency relationship is not continuous.

According to the classification proposed by Izhikevich (2007), bistable dynamical

A. B.

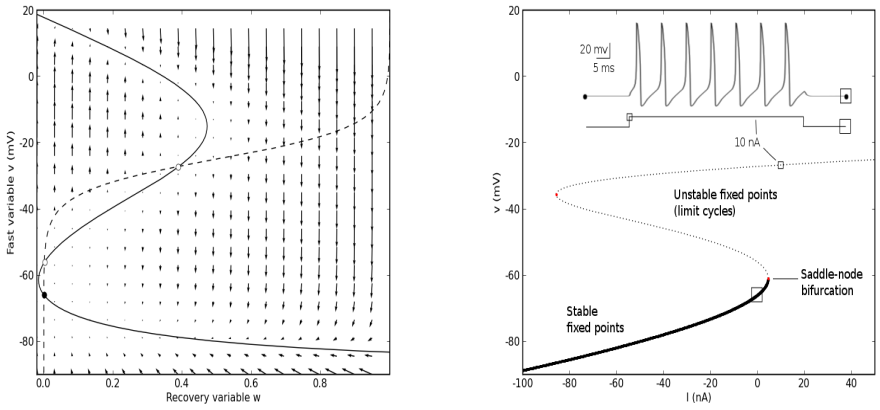

Figure 4.7: Bistable system (4.12)-(4.13) near a saddle-node bifurcation. **A.** Phase portrait showing the vector field and fixed points of the system. The solid dot is a stable fixed point and the empty dots are unstable fixed points. If current is injected into the system, the v-nullcline will shift toward larger values of w (right), bringing the two fixed points with lower v values closer together. **B.** Bifurcation diagram of the system portrayed in A with I as the bifurcation parameter. The dots represent the location of the fixed points for each current level. Thick dots represent stable fixed points and thin dots represent unstable fixed points. A saddle-node bifurcation occurs at approximately $I = 4.51$. At this current level, the two fixed points in the lower portion of the phase plane in part **A** blend together and dissapear for larger I, leaving only one fixed point. This means that for current amplitudes slightly larger than the 4.51, the system will enter into a loop of sustained, periodic oscillations as shown in the insert. Parameters: $l_m = 1 = l_w$, $g_{Na} = 20$, $g_K = 10$ and $g_L = 8$ all in mS/cm^2, $v_{Na} = 60$, $v_K = -90$, $v_L = -80$, $v_m = -20$ and $v_w = -45$ all in mV, $a_m = 0.066$, $a_w = 0.2$, $\tau_w = 1$ ms, $C_m = 1\ \mu F/cm^2$ and $I = 0$. Example from Izhikevich (2007).

systems have excitability of class II. Bistable systems, in turn, can be classified in two groups, integrators and resonators, depending on their bifurcation properties.

One kind of bistability is observed in systems called *integrators* because they are more likely to respond with spikes if the frequency of input increases. Action potentials from these systems are roughly all of the same size. A system becomes an integrator when near to a *saddle-node* bifurcation (Fig. 4.7B), which happens as fixed points are created or dissapear. In this case, a stable fixed point moves closer to an unstable fixed point until they coincide at the bifurcation (one fixed point disapears). The new fixed point is unstable since nearby trajectories start being

repelled along one of the nullclines but not the other, thus forming a saddle-like pattern around the fixed point. The merged fixed point eventually vanishes as I continues to increase. An example of a bistable integrator can be constructed using the same the Hodgkin-Huxley system (4.15)-(4.18) as for the resonator case.

Resonator systems are called like that because their spiking behavior may be restricted to a range of input frequencies, *i.e.,* they can resonate. If the input frequency to the cell is too large or too small, the cell may slow down its rate or completely stop firing. The action potentials from these cells may be of different sizes and it is possible that the membrane potential displays subtreshold oscillations in response to brief stimulation. Resonators may also respond to the release of inhibition. This kind of bistability occurs when the system is near a *subcritical Andronov-Hopf* bifurcation, which occurs when a stable fixed point looses its stability as trajectories converging to it in the form of spirals become cycles that do not reach the fixed point anymore. Another example of the phase portrait of a resonator was shown in Fig. 4.5. The bistability of the system is illustrated by the coexistence of a stable fixed point at $v = -75$ mV and $w = 0.15$ and a stable limit cycle. The basins of attraction for each of the stable states are illustrated, respectively, by the shaded region and the rest of the plane.

4.4.3 Phenomenological models of excitability.

Two systems are *topologically equivalent* if their phase spaces, along with their fixed points and their stability can be transformed into one-another by means of a continous deformation that includes every state in the phase space. In other words, topological equivalence means that there is a one-to-one continuous map with continuous inverse from the phase space of one of the models to the other.

Simplifications of the typical cubic and sigmoidal nullclines from systems like (4.12)-(4.13) can be made so that the system is computationally simpler, or more mathematically tractable. These simplifications amount to constructing topologically equivalent versions of biophysical systems with simpler mathematical expressions. For instance, the w-nullcline can be approximated by a line and the v-nullcline

by a cubic polynomial in v and linear in u. Fitz-Hugh (1961) used this approach to derive the first phenomenological reduction of a Hodgkin-Huxley system. The resulting equations have the form:

$$\frac{dv}{dt} = -v(1-v)(v-a) - w + I \tag{4.19}$$

$$\frac{dw}{dt} = \varepsilon(v - \gamma w) \tag{4.20}$$

where a, I and ε are parameters. The right hand side of (4.19) is indeed a cubic polynomial in v and (4.20) is a linear polynomial in v that approximates the straight part of the sigmoidal w-nullcline. The variable v is scaled so that the equilibrium point is zero, as can be seen from solving for $dv/dt = 0 = dw/dt$. The Fitz-Hugh system has a very small number of parameters and allows a complete characterization of the qualitative aspects related to the generation of action potentials, firing rates, etc.

A less trivial simplification can be made by replacing the v-nullcline by an concave-up parabola (viewed as a function of v) and setting a manual reset for the membrane potential to substitute the portion of the v- nullcline that corresponds to the lower values of v, which in the original model is responsible for starting the downstroke of the membrane potential. One notable instance of this simplification process is the model by Izhikevich (2003), which was derived using a Hodgkin-Huxley system as a starting point and then making the simplifications to the nullclines as described in previous paragraphs. This phenomenological model combines the biological plausibility of biophysical systems with the computational efficiency of integrate-and-fire neurons, enabling the simulation of tens of thousands of spiking neurons in real time (1 ms resolution) using a desktop PC. The resulting expressions for f and g are, respectively, a quadratic polynomial in v and linear in w, and a linear polynomial in both v and w:

$$\frac{dv}{dt} = Av^2 + Bv + C - w + I \tag{4.21}$$

$$\frac{dw}{dt} = a(bv - w) \tag{4.22}$$

with an auxiliary resetting after the occurrence of a spike: if $v \geq \theta$ then $v \leftarrow c$

and $w \leftarrow w + d$, with θ representing a threshold beyond which it is assumed that a spike occurred. The variables v and u (and all the parameters by extension) are nondimensional, so all the terms in the equation merely represent physical quantities by their magnitude, but do not have any units. It can be demostrated by using bifurcation analysis as illustrated above that the case where $b > a$ corresponds to a Andronov-Hopf bifurcation of the resting state (Izhikevich, 2003).

4.5 Models of membrane potential in motor neurons

The concepts illustrated in previous sections are now applied to construct two models of the somatic membrane potential of MNs, one biophysical and one phenomenological. The behavior of the models was shaped first by combining the theory outlined above to with intracellularly recorded properties of MNs (Kernell, 2006).

The list of behaviors in page 16 suggest that MNs are bistable. The bistability comes from the fact that the MN membrane can be attracted to at least two states: rest with no spikes or oscillatory with periodic spiking (see Fig. 4.7). MNs have a well defined current threshold for sustained spiking and may display spikes of different amplitudes while firing repetitively. Taken together, these observations suggest that any dynamical system modeling MN excitability should be near a subcritical Andronov-Hopf bifurcation. Therefore, *mammalian motor neurons can be regarded as bistable resonators.*

4.5.1 MN models.

Two dynamical systems were constructed and constrained by the well known behaviors of MNs listed in subsec. 2.1. The rationale in constructing the models is outlined first, followed by a description of each of the models.

One of the systems was biophysical (Av-Ron et al., 1993) and the other was phenomenological Izhikevich (2003). The biophysical model was created to enable specific questions to be formulated in terms of biophysical properties of the membrane. The phenomenological model was similar to the one described by Izhikevich

(2003) to simulate the membrane potential of mixed-mode or intrinsically bursting cells in cortex. The phenomenological model was chosen to optimize processing time during simulations in which only the input-output properties of the system were relevant. The parameter spaces for each of the models were found using phase plane analysis and bifurcation theory as discussed in Subsec. 4.4.2. Simulations of the dynamics from the two models will be presented showing electrophysiological properties resembling those described in subsec. 2.1.

4.5.2 Biophysical MN models.

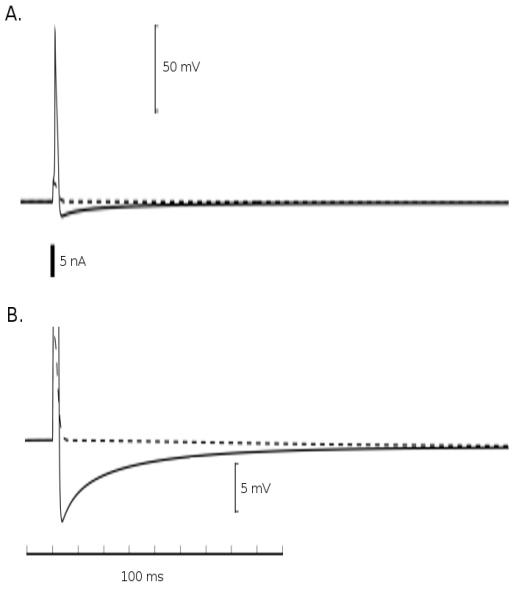

Figure 4.8: Rheobase and afterhyperpolarization of the membrane potential after a spike using the model (4.23)-(4.24). The dashed line shows a current pulse of 4.75 nA in amplitude that fails to trigger an action potential. **A**. Single action potential in response to a short pulse of current. **B**. Amplitude and time course of the after-hyperpolarization in the action potential from **A**. Model parameters: $g_{Na} = 37.5$, $g_K = 45.0$, $g_{Ca} = 0.5$, $g_L = 2.25$, $g_{K,Ca} = 2.0$, $g_S = 30$, in mS/cm^2, $v_{Na} = 55$, $v_{Ca} = 80$, $v_K = -70$, $v_L = -55$, $v_E = 0$, $v_m = -25.75$, $v_n = -32$, $v_s = -39$, $v_q = -42$ mV, $I = 5$ nA, $I_{dur} = 0.2$ ms.

The first biophysical model was a three-dimensional system that includes Eqns. (4.12)-(4.13) in addition to a third slow adaptation variable x representing calcium concentration:

$$C_m \frac{dv}{dt} = I - I_{ion}(v, w, x) \tag{4.23}$$

$$\frac{dw}{dt} = \frac{w_\infty(v) - w}{\tau_w(v)} \tag{4.24}$$

$$\frac{dx}{dt} = \varepsilon\left(-I_{CaL} - r_x x\right) \tag{4.25}$$

The term $I_{ion}(v, w, x)$ in this case was the sum of a fast Na^+-current (I_{Na}), a non-inactivating K^+-current (I_K), a Ca^{2+}-dependent K^+-current ($I_{K,Ca}$), a persistent Ca^{2+}-current (I_{Ca}), a leak-current (I_L) and a synaptic current I_s:

$$I_{ion} = I_{Na} + I_K + I_{K,Ca} + I_{Ca} + I_L + I_s \tag{4.26}$$

defined by

$$\begin{aligned} I_{Na} &= g_{Na} m_\infty^3(v)(1-w)(v - v_{Na}), && (4.27)\\ I_K &= g_K w^4 (v - v_K), && (4.28)\\ I_{K,Ca} &= g_{K,Ca} \left(\frac{x}{k_d + x}\right)(v - v_K), && (4.29)\\ I_{Ca} &= g_{Ca} s_\infty^3 (v - v_K), && (4.30)\\ I_L &= g_L (v - v_L), && (4.31) \end{aligned}$$

with steady state gating functions

$$p_\infty = \left[1 + exp\left(-a_p(v - v_p)\right)\right]^{-1}, \tag{4.32}$$

for $p \in \{m, s, w\}$. The parameters g_{Ca} and k_d are, respectively, the conductance for the Ca^{2+} current I_{Ca} and the rate of removal of Ca^{2+}. The phase portrait of the (fast) subsystem (4.23)-(4.24) was shown in Fig. 4.5. The bistability of the system is illustrated by the coexistence of a stable fixed point at $v = -75$ mV and $w = 0.15$ and a stable limit cycle. The basins of attraction for each of the stable states. are illustrated, respectively, by the shaded region and its complement in the (w, v)-plane.

Since the behavior of the MNs innervating limb muscles in primates does not show burst-like behaviors under physiological conditions, a 2D reduction of the model (4.23)-(4.32) was made by neglecting currents that make small contributions to the membrane potential and assuming that variables that are faster than v were in quasi steady state (Herrera-Valdez and Lega, 2008b). Importantly, the absence of bursting in physiological conditions could be explained by a small, if not negligible contribution of all the persistent Ca^{2+} currents and their K^+ counterparts.

The resulting 2D system is written only in terms of the Na^+-, K^+- and leak currents. The reduced system was defined by (4.23)-(4.24) with I_{ion} replaced by

$$I_{ion} = I_{Na} + I_K + I_L + I_s. \tag{4.33}$$

An example of a simulation using the reduced system is shown in Fig. 4.8. The parameters were tuned so that the rheobase current and afterhyperpolarization were as described in subsec. 2.1 . The parameter ranges were found using phase plane analysis and bifurcation theory so that the system was a bistable resonator (i.e. close to a subcritical Andronov-Hopf bifurcation). The final choice of parameters was made by trial and error.

4.5.3 Phenomenological MN model.

The phenomenological model of MNs was very similar to the one already described by Eqs. (4.21)-(4.22).

$$\frac{dv}{dt} = Av^2 + Bv + C - w - I_s + I \tag{4.34}$$

$$\frac{dw}{dt} = a(bv - w) \tag{4.35}$$

with an extra term I_s representing the contribution of synaptic current to the membrane potential. The system (4.34)-(4.35) is very convenient for simulations where the input-output properties of the system are a priority.

The parameters A, B, C, a, b, c and d can be set to match firing properties of different neuronal classes (Izhikevich, 2004). For instance, the sought MN behavior for our nearly coincident spiking model is displayed by choosing $A = 0.04, B = 4.1, C = 108, a = 0.01, b = -0.2, c = -55.0$ and $d = 10.0$. These parameters are very similar to those proposed by Izhikevich to reproduce intrinsically bursting behavior (Izhikevich, 2004).

The behavior of the model MNs in response to a short pulse of current injection is shown in Figs. 4.9. Note that the phenomenological model (4.34)-(4.35) actually responds with doublets and tripplets for large pulses of current injection as shown in Fig. 4.10.

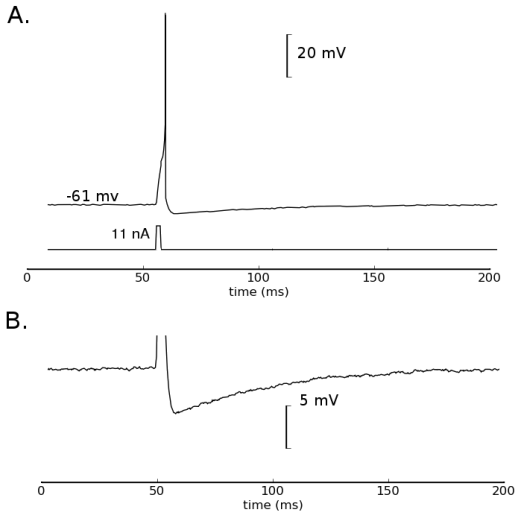

Figure 4.9: Rheobase and afterhyperpolarization of the membrane potential after a spike using the model by Izhikevich (2003). **A**. Single action potential in response to a short pulse of current. **B**. Amplitude and time course of the after-hyperpolarization in the action potential from **A**. Model parameters: $A = 0.04$,$B = 4.1$, $C = 108$, $a = 0.01$, $b = -0.2$, $c = -55.0$, $d = 10.0$, $I = 10$, $I_{dur} = 18$ ms. Noise was injected as direct current with a maximum amplitude of 0.5 nA.

4.5.4 Modeling synaptic input to MNs

Experimental data obtained from intracellular recordings in MNs responding to the stimulation of single presynaptic axons indicates that any given presynaptic spike triggers EPSPs of different amplitudes from spike to spike (Burke, 1967; Shapavalov et al., 1971; Jankowska et al., 1975; Redman and Walmsley, 1983b). The range of amplitudes across different types of synaptic inputs (*e.g.,* corticospinal, rubrospinal, Ia afferent) is approximately 0.025 to 1.2 mV. One factor contributing to this phenomenon is that each input axon makes multiple synapses onto the target MNs (Redman and Walmsley, 1983b). Also see Jankowska et al. (1975) and contrast with Asanuma et al. (1979). In turn, the arrival of one presynaptic spike activates each of the synapses made by the input cell depending on a probability of activation, as it is the case for the Ia-afferents (Walmsley et al., 1988). The peak conductance amplitude for the nth synapse, a_n, can thus be assumed to behave as a Bernoulli random variable taking a nonzero value with probability p_n and zero with probability $1 - p_n$. The somatic EPSPs triggered by input spikes were modeled assuming that each input axon makes several synapses with a target MN. Following an input spike, activation of the nth synapse occured after a conduction delay δ_n with a probability p_n. After each input spike, the EPSPs triggered at the activated synapses were integrated, resulting in composite EPSPs of different amplitudes. The composite

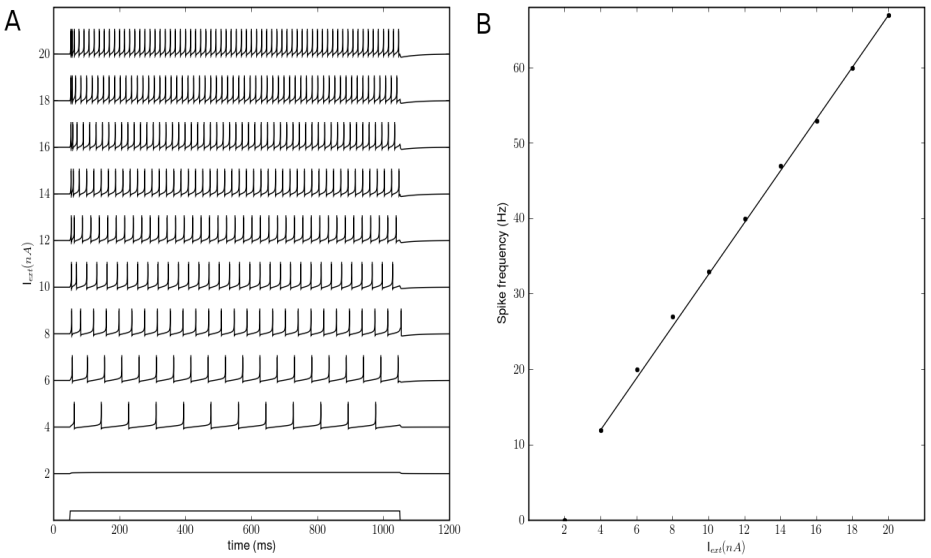

Figure 4.10: MN model response to current injection. Note the appearance of doublets when the applied current I_{app} is increased Bawa and Calancie (1983). Importantly, note that repetitive firing is not evoked until the external current has reached about 4 nA. The range of firing frequencies corresponds to experimentally observed values (Kernell, 1965c, 2006, Ch 6). The system used in this simulation was (4.21)-(4.22) with parameters as in 4.9: $I \in [0, 20]$, $I_{dur} = 1000$ ms.

EPSP triggered by an input spike will have the maximum possible amplitude only if all the synapses made by the carrying axon are activated.

In more detail, the time course of the *conductance amplitude* at the nth synapse was defined by an alpha-function as described by Kuhn et al. (2004):

$$A_n(s) \quad = \quad a_n I_{\{x_t < p_n\}} \frac{s}{\tau_n} exp\left(1 - \frac{s}{\tau_n}\right) H(s), \tag{4.36}$$

where s is the time of activation of the synapse, a_n is the peak synaptic conductance, I_X is an indicator function, equal to 1 if X occurs and 0 otherwise, τ_n is the time constant of the conductance transient and $H(s)$ is the heaviside function, equal to 1 if $s > 0$ and 0 otherwise (Fig. 4.11).

Synaptic activation was simulated by choosing a random number x between 0 and 1 each time a spike arrived at the nth presynaptic terminal. If $x < p_n$, where p_n is the probability of synaptic activation, then a_n takes a nonzero value (Redman

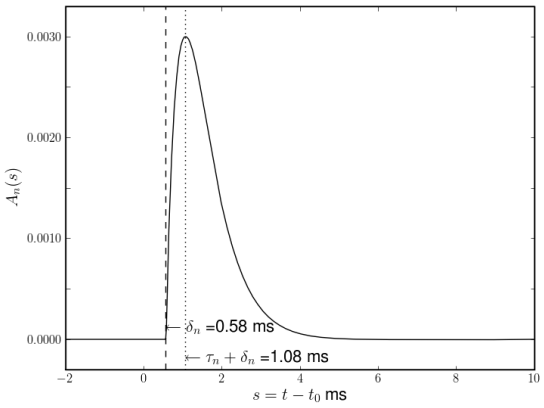

Figure 4.11: Alpha function representing the synaptic conductance relative to a spike time t_0 with parameters $a_n = 0.003$, $\tau_n = 0.5$ ms, $\delta_n = 0.58$ ms.

and Walmsley, 1983a; Walmsley et al., 1988). For instance, if an input spike is generated at time t_0 and the spike arrives to the presynaptic terminal n after some conduction delay δ_n, then the amplitude of the postsynaptic conductance transient is $A_n(t - t_0 - \delta_n)$. Note that A_n will be zero for $t < \delta_n + t_0$ and positive after $\delta_n + t_0$ with an exponential decay at a rate τ_n after $t = \delta_n + t_0 + \tau$.

The conductance observed at a single synapse at time t as the sum of all the conductance transients triggered at times $t_1, ..., t_M$:

$$G_n(t) \quad = \quad \sum_{m=1}^{M} A_n(t - t_m - \delta_n), \tag{4.37}$$

where $(t - t_m - \delta_n)$ is the time lapsed from the occurence of the mth input spike after some delay δ_n (Fig. 4.12). The delay δ_n accounts for the conduction delay within the presynaptic axon to the sth synaptic terminal. The delay accounts for conduction velocities within the the grey matter ranging between 1 and 4 m/s (Asanuma et al., 1979), assuming a maximum dendritic distance of 1.5 mm (Segev et al., 1990).

A simplification supported by the data collected by Redman and Walmsley (1983a), was made by assuming that all the synapses made by a single input cell onto a MN are independently activated and that the parameters p_n, δ_n, τ_n and a_n for all the synapses made by an input axon have the same values, respectively, p_s, δ_s, τ_s and a_s. The common value for each of the parameters was set as the average calculated for all synapses from the same axon. This assumption allows a

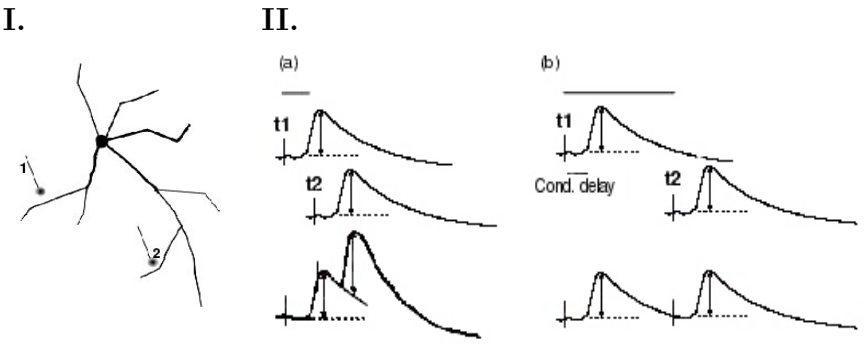

Figure 4.12: Integration of postsynaptic conductance responses. **I.** Schematic representation showing two excitatory synapses onto a target MN. **II.** Temporal summation of somatic conductance transients calculated from Eqn. (4.36). The conductance trainsients are triggered by spikes occurring at times t_1 and t_2 after conduction delays δ_1 and δ_2 respectively. (a) If the delay $t_2+\delta_2-(t_1+\delta_1)$ between the trigger spikes is short enough, the resulting conductance transients will add up. (b) If the trigger spikes are very distant in time, the conductance transients will not have an influence on one another. The multiple EPSP amplitudes observed in MNs in response to the stimulation of the same presynaptic axon (Shapavalov et al., 1971; Jankowska et al., 1975; Redman and Walmsley, 1983a) is likely to result from integration of synaptic inputs as shown in (a) and are assumed to occur this way in the model. In this case, the presynaptic terminals schematized in **I** would belong to the same axon.

great reduction in simulation time, and yields composite EPSPs resembling those experimentally observed; simulations were done before and after this simplification, yielding no apparent differences in the overall qualitative behavior of the system with respect to firing rates, coefficients of variation in ISIs, etc. One consequence of this simplification is that, for each input axon, the simulation of several Bernoulli processes (one for each synapse), is replaced by a simulation of an equivalent binomial process in which the peak conductance for the composite EPSP is obtained. In this simplified scheme, a random number representing the newly activated synapses is drawn after each input spike and multiplied by the common peak conductance.

For instance, if an input spike occurs at time t_0, activating N synapses, then the composite conductance amplitude will have a peak value of $N \cdot a_s$ (Fig. 4.13A). The time course of the composite conductance in response to an input spike is:

$$\bar{A}_n(\tilde{t}) \;=\; N a_s \frac{\tilde{t}}{\tau_n} exp\left(1-\frac{\tilde{t}}{\tau_n}\right) H(t), \tag{4.38}$$

where $\tilde{t} = t + t_0 + \delta_s$ is the time relative to the occurrence of the input spike t_0 after the common conduction delay δ_s. An equivalent circuit justification for this approximation can be made by observing that the total conductance resulting from an array of parallel conductors is the sum of the individual conductances.

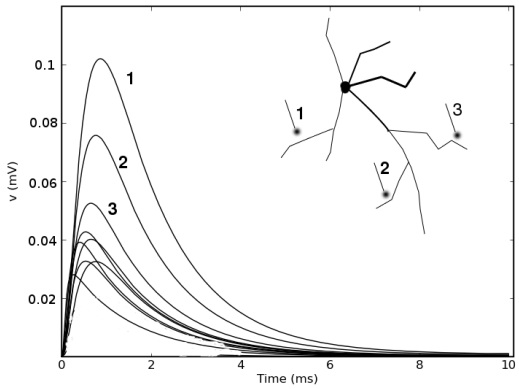

Figure 4.13: Synaptic integration in the MN model. The insets show a schematic MN with three different synapses in each case. Different amplitudes of single-synapse EPSPs triggered in a model MN in response to input spikes from different axons. The smaller EPSPs represent the minimum EPSP amplitude triggered in the MN in response to the activation of one synapse.

To get maximum postsynaptic responses equivalent to 1.4 mV, the maximum number of synapses per axon was set to 12, the peak synaptic conductance, $a_s = 0.003$, and the conductance time constants τ_s were sampled uniformly from the interval $[0.1, 0.5]$ ms. These values guaranteed that the single-synapse EPSPs were not larger than 100 μV but no smaller than 25 μV (Fig. 4.13A). Sampling the probability of synaptic activation per axon p_s uniformly from the interval $[0.1, 0.75]$, the *composite EPSPs* had a maximum peak amplitude of about 1.4 mV and a minimum peak amplitude $\sim 25\mu$V, (Fig. 4.13B).

Taken the above definitions into consideration, the right hand side of the equation for v will include a term I_s representing synaptic current:

$$I_s \;=\; G_{syn}(t)(v - v_{syn}). \tag{4.39}$$

where v_{syn} is the excitatory reversal potential and $G_{syn}(t)$ is the total synaptic conductance. The total synaptic conductance is the sum of all the single synapse conductances, $\bar{A}_n(t)$, for $n = 1, ..., N_a$ where N_a is the number of input axons making synapses onto the MN. Experimental data from Jack et al. (1981) are shown in Fig. 4.14A. Examples of the distributions of composite EPSP amplitudes corresponding to single input axons are shown in Fig. 4.14B.

A.

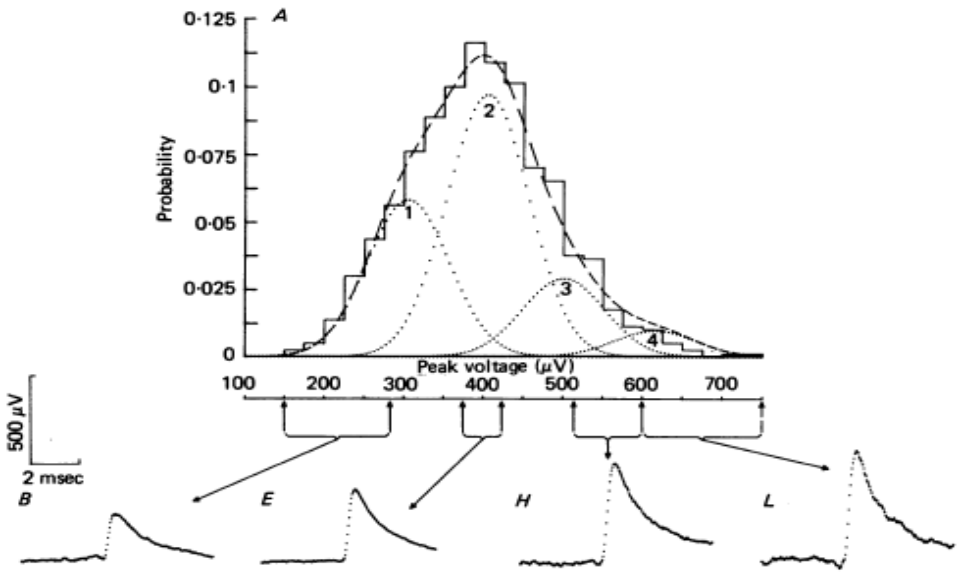

B.

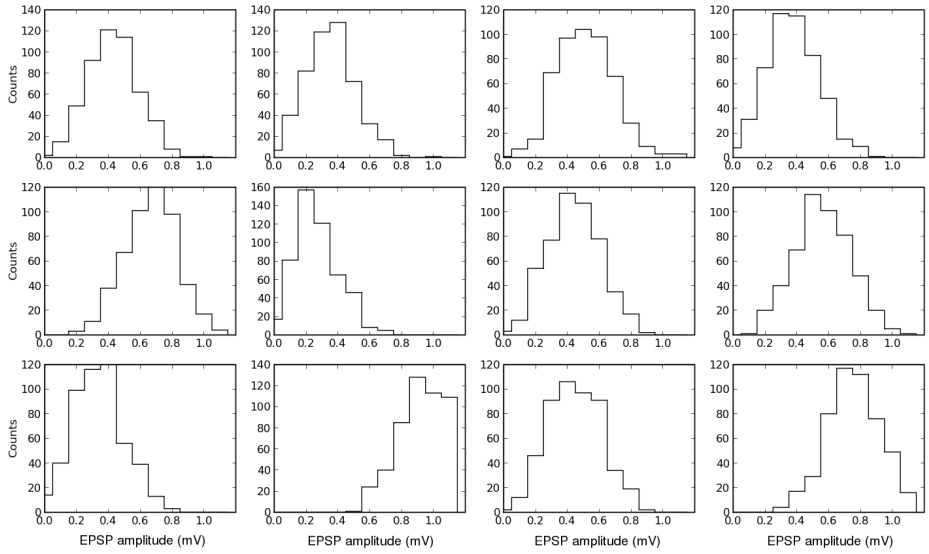

Figure 4.14: **A.** Distribution of peak EPSP amplitudes from a single presynaptic axon obtained experimentally by Jack et al. (1981). **B.** Sample of simulated somatic EPSP amplitudes. Each distribution corresponds to the EPSP amplitudes triggered by spikes from the one presynaptic axon.

4.5.5 Spike trains from input neurons

The input spikes to MNs were generated as realizations of renewal stochastic processes as explained in subsec. 4.3 and illustrated in Fig. 4.2C-D. The sampling time step was 1 ms and the refractory period 2 ms. The firing rates were adjusted to simulate high frequency synaptic drive and obtain a preliminary idea of the output responses of the model MNs.

4.5.6 Predictions from the construction of the model.

The average conductance amplitude underlying a composite EPSP triggered by an input axon can then be approximated by noticing that the expected number of active synapses after each spike is the product of the maximum number of synapses, N_s and the common probability of synaptic activation p_s. Then, conductance transient following an input spike $\bar{A}_{in}$ can be approximated by the average:

$$\bar{A}_{in}(t) \;=\; (N_s p_s) \cdot A(t). \tag{4.40}$$

where A is the conductance amplitude given by equation (4.36). In this simplified scheme, the average conductance transient for each input axon replaces the different conductance transients that result after each input spike. This prediction was used to estimate the number of inputs supplying the MNs required to drive the MNs to spike at frequencies similar to those observed in experiments (7-18 Hz). Full simulations done later confirmed that the estimates were correct (see Fig. 4.15).

The range of the *number of input axons*, N_a, was found by running simulations with increasing values of N_a, until the firing rates of the model MNs were physiologically realistic. Fig. 4.15 illustrates simulations where the discharge frequencies were within the range 7-18 Hz as observed in primate motor units controlling distal upper limb muscles Nordstrom et al. (1992). The model predicts that N_a must be between 250 and about 450 with a firing rates between 10 and 50 Hz, in order that upper limb MNs fire between 7 and 18 Hz. This range is very similar to estimations about synaptic input to MNs made by Segev et al. (1990) and Kernell (2006).

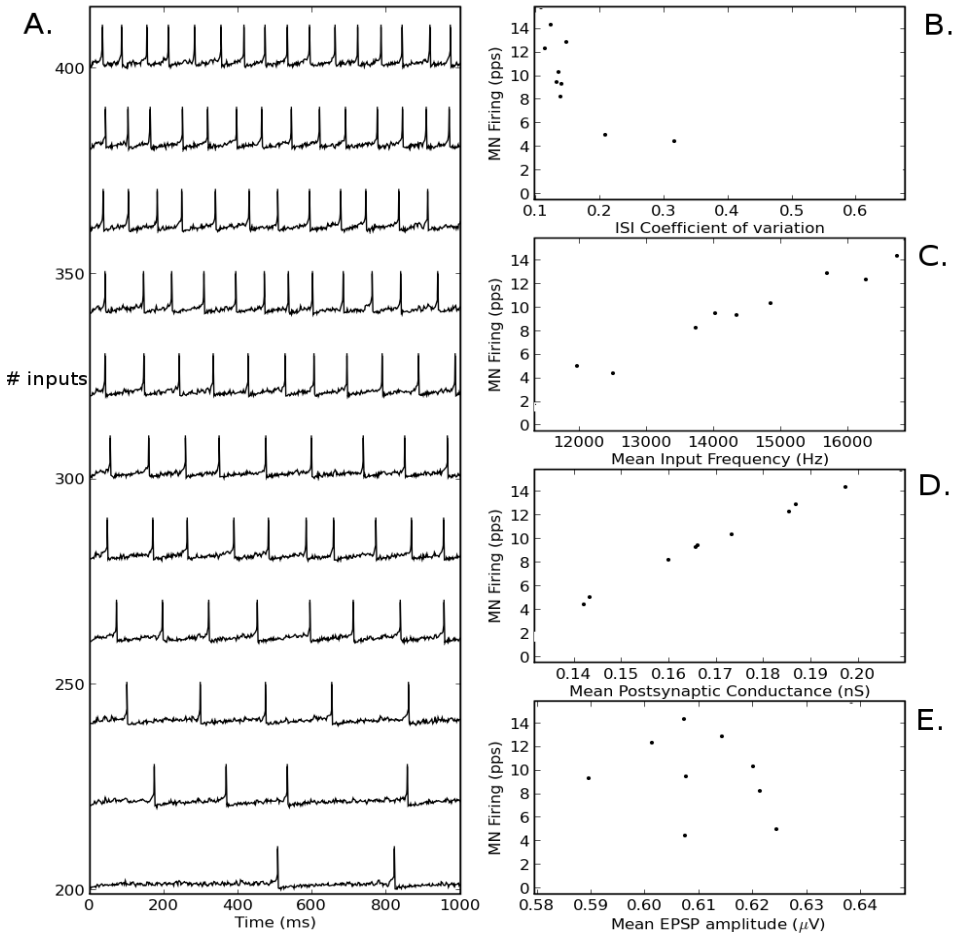

Figure 4.15: Range for the number of inputs required to drive the model MNs to have average instantaneous frequencies between 7 and 15 Hz, a range similar to the experimentally observed in recordings of hand and forearm motor units (Nordstrom et al., 1992). **A.** Membrane potential dynamics for an increasing number of input axons. **B.** Firing rate vs the coefficient of variation of interspike intervals ν_{isi}. **C.** Firing rate vs the input frequency $\bar{\omega}_{in}$ (Hz). **D.** Firing rate vs mean postsynaptic conductance $\bar{G}_{syn}$. **E.** Firing rate vs single synapse EPSP amplitude (μV).

In simulations when the MN fired between 7 and 17 Hz with p_s in the interval $[0.1, 0.75]$, the coefficient of variation of the MN interspike intervals, ν, was between 0.1 and 0.35, in agreement with experimentally observed values (Fig. 4.15B). Furthermore, ν was seen to increase with low rates of spiking as is seen experimentally (Person and Kudina, 1972; Piotrkiewicz, 1999; Powers and Binder, 2000). To assess the behavior ν in terms of synaptic activation, simulations were carried out where the ranges for the probability of synaptic activation, p_s were 0-0.25, 0.25-0.4, 0.4-0.6 and 0.6-0.75, while other synapse-related parameters were kept constant (not shown). The effect of increasing the probability of synaptic activation was to shift the distributions from Fig. 4.14B to the right, causing larger EPSPs per input axon. ν increased from the range 0-1 to ranges approximately 0.1-0.175, 0.125-0.2 and 0.15-0.25, respectively. In addition, these ranges for p_s will be used to study nearly coincident spiking in MN pairs with possibly different recruitment thresholds; the rationale being that EPSP amplitudes in neurons with lower recruitment thresholds should be, on average, larger than EPSP amplitudes in MNs with higher recruitment thresholds, due to differences in input resistance.

As expected, the mean input frequency $\bar{\omega}_{in}$ and the time-averaged total synaptic conductance $\bar{G}_{syn}$ increased with N_a (Fig. 4.15C-D). The average firing rate of the MN was monotonically increasing with respect to N_a. Similarly, if the maximum number of synapses per input axon increased while all other variables remained the same, then the firing frequency of the MN increased, at least within the limits described here. As predicted for the present model, the average (all axons) EPSP amplitude in MNs showed no systematic change with increased synaptic drive (Fig. 4.15E).

4.6 Overview.

The information provided up to this point is sufficient to construct a comprehensive, yet, basic model of simultaneous spiking activity in motor neurons that includes synaptic input. Chapter 5 describes the construction of a model in which motor neu-

rons receive common, yet uncorrelated excitatory synaptic input that links different schemes of common excitatory synaptic drive to simultaneous spiking activity in motor neurons.

Appendix: From Binomials to Poisson. Notation:

$$\binom{n}{k} = \frac{n!}{(n-k)!k!} \tag{4.41}$$

Asumptions:

1. The neuron has an average firing rate r, so that the probability of a single spike to occur in a small interval of length δ_t is approximately equal to $p = r\delta_t$. That is $P[\text{single spike within } \delta_t \text{ seconds}] = r\delta_t + o(\delta_t)$.

2. The probability of more than one spike in a small time interval of length δ_t is negligible when compared to the probability of just one spike in the same time interval. That is $P[\text{Two or more spikes in an interval of length } \delta_t] = o(\delta_t)$.

3. Any two spikes will occur independently in nonoverlapping intervals; just as if at each sampling time, a spike occurred depending on the toss a coin.

The term $o(\delta_t)$ is read "some function of smaller order than δ_t" denotes an unespicified function which satisfies $lim_{\delta_t \to 0} o(\delta_t)/\delta_t = 0$.

$$\begin{aligned} P\left(k \text{ spikes before } T\right) &\approx \frac{n!}{(n-k)!k!} p^k (1-p)^{n-k} \\ &= \frac{p^k}{k!} \cdot \frac{n!}{(n-k)!} (1-p)^{n-k} \\ &= \frac{(rT)^k}{k!} \cdot \frac{n!}{n^k (n-k)!} \left(1 - \frac{rT}{n}\right)^{n-k} \end{aligned} \tag{4.42}$$

If we let n tend to infinity,

$$\frac{n!}{n^k(n-k)!} = \frac{n(n-1)\cdots 2 \cdot 1}{n^k (n-k)(n-k-1)\cdots 2 \cdot 1} \quad \to \quad 1 \tag{4.43}$$

$$\tag{4.44}$$

and

$$(1-p)^n = \left(1-\frac{rT}{n}\right)^n \left(1-\frac{rT}{n}\right)^{-k} \quad \rightarrow \quad exp\,(-rT) \tag{4.45}$$

In consequence,

$$\frac{n!}{n^k(n-k)!}\,(1-p)^{n-k} \quad \rightarrow \quad exp\,(-rT)\,. \tag{4.46}$$

and therefore

$$P\,(k \text{ spikes before } T) \quad \rightarrow \quad \frac{(rT)^k}{k!} exp\,(-rT) \tag{4.47}$$

as $n \rightarrow \infty$.

Chapter 5

Relationship between common excitatory input and nearly coincident siking in spinal motor neurons receiving common excitatory synaptic input.

5.1 Introduction

The information provided in previous chapters is sufficient to construct a physiologically tractable model of spiking motor neurons that enables an investigation of the link between common synaptic excitatory drive and nearly-coincident spiking. One of the motivations to construct such a model is to test hypotheses advanced by Sears, Stagg and Kirkwood regarding common synaptic input and nearly coincident spiking (see chapter 2, on page 13). The relationship between the correlated excitatory input and the spike timing of their targets has been extensively studied in simplified models of cortical networks (Ermentrout and Kopell, 1998; Kopell et al., 2000; Kumar et al., 2008) and more recently, by combining experimental and theoretical approaches (de la Rocha et al., 2007; Markowitz et al., 2008). However, in spite of the common interpretation of central peaks in correlograms from motor units as indicative of common presynaptic inputs to the underlying motor neurons, the question of how the correlation function between two spike trains is influenced by the degree of common synaptic excitatory drive to the underlying neurons, regardless of any correlation in the input spikes, has not been thoroughly investigated in vertebrate systems (Nielsen et al., 2005) (but see Gilchrist and Mesche, 1997; Johnston et al., 1998), or has been approached in theoretical studies that have certain limitations (Binder and Powers, 2001; Taylor and Enoka, 2004). In particular, realistic synaptic input has not been part of the construction in any of the above models.

Therefore, a feed-forward excitatory network model was developed that was composed of two layers of neurons: one layer representing corticospinal neurons provid-

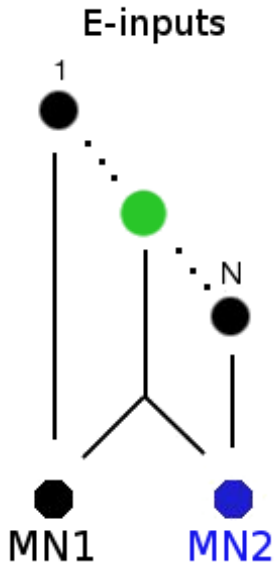

Figure 5.1: Schematic diagram illustrating the overall organization of the model. A total of N excitatory (E) sources provide common (green) or isolated (black) synaptic inputs to two MNs. The activity of the input sources are themselves uncorrelated.

ing distributed excitatory inputs to the second layer, representing MNs. The model was designed to be physiologically realistic while also computationally tractable.

5.2 Methods

Construction of the model. The model consists of two layers of neurons. The first layer constitutes the input of the system and can be thought of as a bundle of corticospinal axons that make excitatory synapses onto a pair of motor neurons that comprise the second layer. A simple scheme illustrating the general setup of the model is shown in Fig. 5.1.

The input layer had hundreds of cells spiking simultaneously but independently. Their pattern of activity was selected to mimic corticospinal input to MNs. The synaptic drive from the input layer was assumed to be uncorrelated and there was no synaptic coupling between neurons within any of the layers. Consequently, the only correlations displayed by the spikes in the motor neurons were those resulting from common input. Cells within the same layer were not synaptically coupled. Both MNs received excitatory synaptic input from N_a cells in the input layer. In each simulation, a subset of cells in the input layer made synaptic contact with

both MNs (Asanuma et al., 1979; Shinoda et al., 1981; Lawrence et al., 1985). The proportion of common excitatory input, p_c, was defined as the ratio N_c/N_a.

Each input axon was assumed to make up to 12 synapses onto its target MN to match the maximum EPSP amplitudes reported by Shapavalov et al. (1971), Jankowska et al. (1975), and Redman and Walmsley (1983b). As such, somatic single-synapse EPSPs ranged between 25 and 100 μV, for a maximum of composite EPSP of ≈ 1.4 mV. Each synapse had its own delay, probability of activation, peak conductance, and time constant. Therefore, each input spike from a single axon triggered conductance transients in a random number of synapses, thereby causing the total synaptic conductance of the cell to increase by different amounts (Burke, 1967; Shapavalov et al., 1971; Jankowska et al., 1975; Redman and Walmsley, 1983b). The total synaptic conductance was obtained by adding the conductances from all synapses.

Spike trains from input neurons. The synaptic drive to MNs was composed of hundreds of spike trains generated as realizations of renewal processes as explained in subsec. 4.3 and illustrated in Fig. 4.2C-D. The sampling time step was $\delta = 1$ ms, the refractory period $\rho = 2$ ms, and the average firing rate r was between 10 and 50 pps, as observed in corticospinal neurons during sustained voluntary contractions Cheney and Fetz (1980).

Spiking activity in the input layer triggered the occurrence of excitatory post-synaptic potentials (EPSPs) in the MNs. The integrated response of the MN to synaptic drive caused, in turn, the occurrence of spikes in the MNs.

In the interest of minimizing the computational cost of the simulations, the results presented in this chapter only include simulations obtained using the phenomenological model (4.21)-(4.22). Simulations were performed using C. The code is available upon written request to Marco A. Herrera-Valdez and Andrew J. Fuglevand.

The model MNs were constrained to simulate the properties of mammalian MNs (see chapter 4). That is, the model was bistable and near a subcritical Andronov-Hopf bifurcation. The parameters from the resulting dynamical system were further

constrained by trial and error to have specific responses in amplitude and spike frequency in agreement with a number of well established properties observed from intracellular recordings of MNs as described in chapter 4.

The membrane dynamics of the model MNs were given by:

$$\frac{dv}{dt} = Av^2 + Bv + C - w - I_s(v) + I, \tag{5.1}$$

$$\frac{dw}{dt} = a(bv - w), \tag{5.2}$$

with an auxiliary resetting after the occurrence of a spike: if $v \geq \theta$ then $v \leftarrow c$ and $w \leftarrow w + d$, with θ representing a threshold beyond which it is assumed that a spike occurred. The variables v and u (and all the parameters by extension) are non-dimensional, so all the terms in the equations merely represent physical quantities by their magnitude, but do not have any units. The parameter I represents the current applied though an electrode. The term I_s represents the total synaptic current as defined earlier. For simplicity, most variables and parameters from the model will be referred to as "potentials", "conductances", "currents", etc. The parameters A, B, C, a, b, c, and d can be set to match firing properties of different neuronal classes (Izhikevich, 2004), making it very convenient for simulations where the input-output properties of the neurons are a priority. For instance, the sought MN behavior for our nearly-coincident spiking model is displayed almost from the outset by choosing $A = 0.04$, $B = 4.1$, $C = 108$, $a = 0.01$, $b = 0.2$, $c = -55.0$, and $d = 4.0$ (Figs. 4.9 and 4.10). These parameters are very similar to those proposed by Izhikevich to reproduce intrinsically bursting or multi-mode behavior (Izhikevich, 2003).

Simultaneous spiking activity of the MNs was quantified by calculating the raw correlation function of their spike trains, *i.e.,* by counting the number of spikes occurring in one MN at different delays from spikes in the other MN. The presence of central peaks in the corresponding correlograms was assessed and quantified with the experimentally deployed indices of coincidence CIS and k (see Ch. 3). The relationship between common synaptic input and the indices CIS and k was quantified as the proportion of common inputs to both cells, p_c was systematically increased.

In addition to assessing the behavior of CIS and k assuming that the MNs were receiving inputs with the same distribution of firing rates and had statistically similar probabilities of synaptic activation in their synapses, two specific manipulations were carried out to investigate the behavior of the indices CIS and k when either the input, or the output properties of the MNs changed. The first manipulation involved altering the range for the probability of synaptic activation, and the second involved varying the range for the firing rates of the input neurons.

More specifically, the following simulations were carried out:

1. First, the relationship between the likelihood that two MNs respond to excitatory synaptic input and the coincidence indices CIS and k was studied by assuming that both the input and the output properties of the two MNs were statistically the same (subsec. 5.3.1).

2. Next, simulations were carried out assuming that the EPSP amplitudes of one MN were statistically larger than those of the other MN. The firing rates of the inputs were the same for both MNs. The data from these simulations can be thought of as recordings obtained from pairs of MNs with different recruitment thresholds (subsec. 5.3.2).

3. The influence of the input frequency on the joint-spiking of MNs was studied in simulations where the number of input neurons, N_a, was systematically increased. The firing rates of the inputs to both MNs and the amplitudes of the resulting composite EPSPs were statistically indistinguishable for both neurons. The output firing frequency of the MNs was thus increased due to the increased number of input axons (subsec. 5.3.4).

5.3 Results

Figure 5.2 shows example response properties of the model. Sample raster plots of the input spike trains are shown in Fig. 5.2A. Examples of somatic EPSPs in a single MN in response to input from a single pre-synaptic axon are shown in Fig.

5.2B. The resulting membrane potential dynamics in the two MNs in response to the synaptic input shown in Fig. 5.2A are shown in Fig. 5.2C.

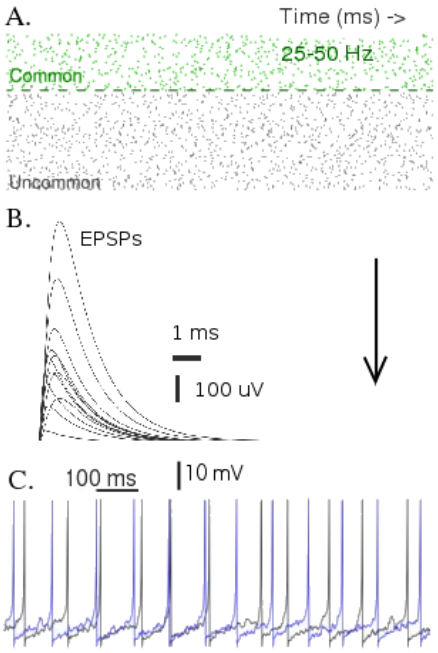

Figure 5.2: Spiking characteristics of the cells in the model. **A.** Sample raster plot with input spike trains. The dashed line separates common and the uncommon input spikes. In this example, the firing rates of the inputs were between 10 and 50 Hz. **B.** Sample of somatic EPSPs in a single MN in response to the spikes from a single input cell. The maximum amplitude is ≈ 1.2 mV. The time to peak varied between 0.5 and 1.5 ms. **C.** Sample of the membrane potential dynamics from the two model MNs in response to the inputs shown in B.

5.3.1 Nearly-coincident spiking between MNs with statistically similar EPSP amplitudes

Every simulation presented in this section was carried assuming that all the parameters were uniformly sampled from the same intervals for both neurons ($N_a = 250$, $0 \leq p_c \leq 1$, $r \in [10, 50]$ pps). Thence, the synaptic drive to the MNs was expected to be equivalent from simulation to simulation. Different statistics from the MN spike trains were calculated to check that the simulations were robust and that the results reported here depend only on the manipulation of the common excitatory input. Fig. 5.3 illustrates the resulting coefficients of variation and average firing rates (Fig. 5.3B) as a function of common input for 215 simulations. The coefficients of variation (Fig. 5.3A) and the average firing rates of the MNs were approximately constant with average values 0.21 $\pm$0.01 and 12 ± 2 pps respectively, in agreement with values reported in the literature.

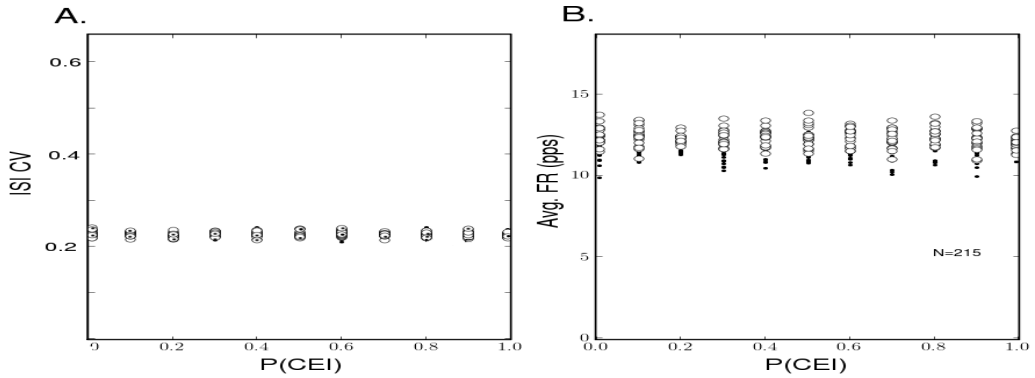

Figure 5.3: Different quantifications of the spiking displayed by the model MNs for different levels of common excitatory input. The reference MN in each pair is shown in solid dots, and the response neuron in open circles. **A.** Coefficient of variation of the interspike intervals. **B.** Mean firing rate in the model MNs in function of p_c. In all simulations shown $N_a = 250$, $\rho \in [10, 50]$ pps, $p_s \in [0.1, 0.75]$, $\tau_s \in [0.075, 0.5]$, $a_s = 0.003$.

Fig. 5.4 shows the results from 269 simulations where p_c, the proportion of common input, was increased from 0 to 1. Each panel shows the correlograms from approximately 20 simulations in which p_c was constant. The duration of each trial was 100 seconds. Each of the correlograms is represented by a trace of different color. The average correlogram from all the simulation is plotted in black. The top inset in each panel shows a normalized version of the central cumulative sum used to detect the limits of central peaks. The color traces of cumulative sum correspond to the correlograms shown below and the black line is the average of all cumulative sums for each condition. The bars highlighting the region around time-delay zero delimit the average peak region. In general, the height and to a lesser degree the width of the central peaks increased with p_c. Simulations for $p_c < 0.2$ did not show any prominent central peaks. On the other hand, for $p_c > 0.2$ central peaks became noticeable and very large as p_c was closer to 1.

Secondary peaks in the correlogram emerged in simulations where the firing rates of the two neurons were similar, as is the case in the simulations presented so far. Interestingly, when common input was increased the secondary peaks (at a time shift of about 80 ms) became more prominent. The time lag to these secondary

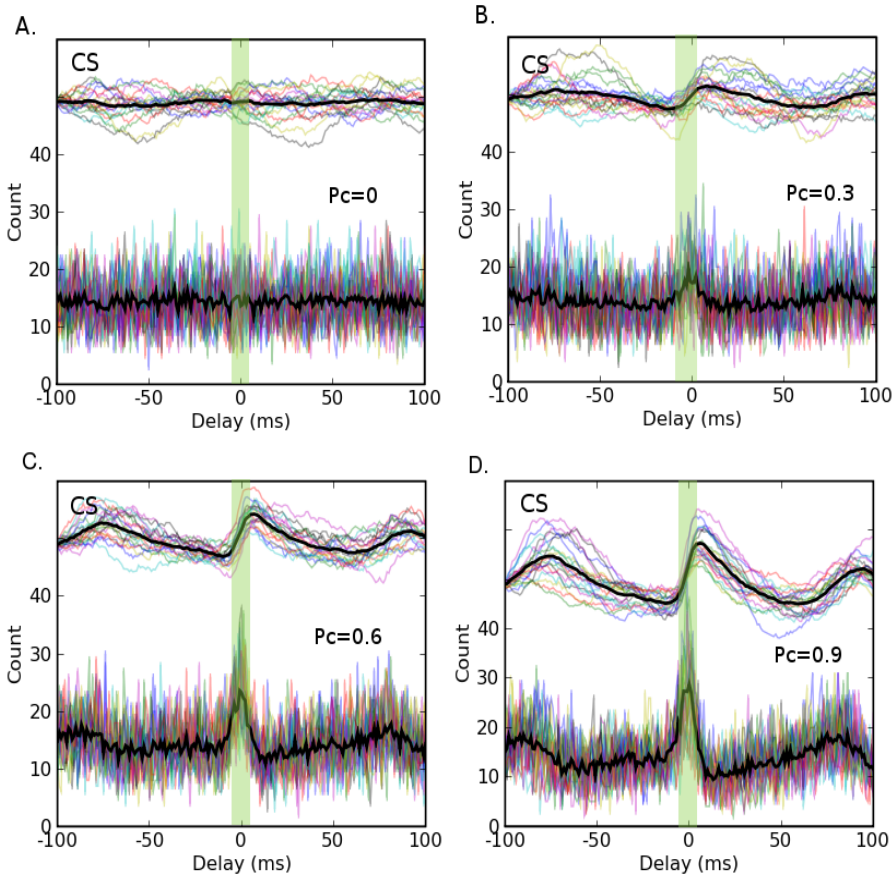

Figure 5.4: Four examples of correlograms obtained from simulations where $p_c \in \{0, 0.3, 0.6, 0.9\}$. The simulations for each value of p_c are shown in parts **A-D**. The color traces in the lower portion of each panel represent joint spike counts for 20 different trials, with the overlaid black line showing the average of the correlograms. The top insets in each panel show normalized central cumulative sums. The interval containing the average peak is illustrated by a (green) vertical band. In all simulations shown $N_a = 250$, $\rho \in [10, 50]$ pps, $p_s \in [0.1, 0.75]$, $\tau_s \in [0.075, 0.5]$, $a_s = 0.003$.

peaks is similar to the average interspike intervals of the trains

Central peaks were quantified by means of the coincidence indices CIS and k. Each index was calculated using two different methods to detect the region in the correlograms where nearly-coincident spiking occurred. There was a remarkable similarity between the simulated and the experimentally reported values for both CIS and k (see Table 5.1). For instance, CIS values for pairs of motor units have been reported to span the range between 0 and 2.5 (Nordstrom et al., 1992; Semmler

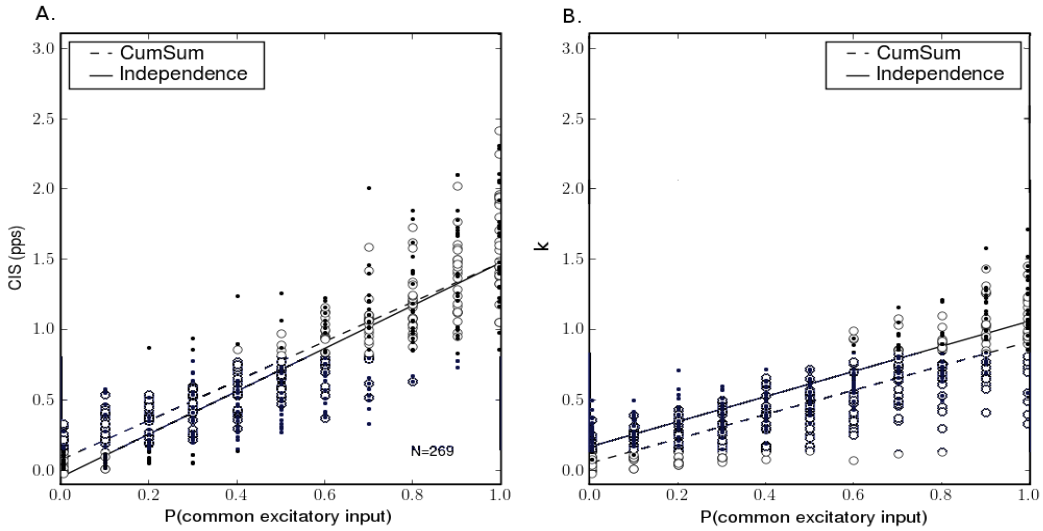

Figure 5.5: The strength of NCS measured using two indices, CIS and k. Central peaks were found using the central cumulative sum Ellaway (1978). The dashed lines and open circles show the results obtained using the cumulative sum method to detect the central peak. The solid lines and dots represent values based on using the correction for independence to detect the central peak. **A.** CIS as a function of p_c. **B.** k as a function of p_c. From the simulations shown in Fig. 5.4. In all simulations shown $N_a = 250$, $r \in [10, 50]$ pps, $p_s \in [0.1, 0.75]$, $\tau_s \in [0.075, 0.5]$, $a_s = 0.003$. See Table 5.1 for experimental values.

et al., 2003; Keen and Fuglevand, 2004; McIsaac and Fuglevand, 2007). The scatter plots in Fig. 5.5 show results of these analyses.

Fig. 5.5A and B show, respectively, CIS and k calculated from a set of simulations that included those shown in Fig. 5.4, done for different proportions of common input between 0 and 1. The results using the widely adopted cumulative sum method (Ellaway, 1978, defined on page 36) are illustrated by open circles and linear regression best fit is shown with dashed lines. The results obtained using the correction for independence (see 3.10) are shown with dots and solid linear regression lines. Both indices, CIS and k increased linearly as functions of p_c. CIS values were in the interval (-0.05,2.45) when calculated with the cumulative sum method and in (0.025,2.35) when calculated with the correction for independence. The variability increased in both indices for larger values of p_c, suggesting that the relative amplitudes of the central correlogram peaks with respect to the baselines

Table 5.1: CIS and k values obtained experimentally from different human hand muscles. Abbreviations: FDP flexor digitorum profundus, FDS flexor digitorum superficialis, DI Dorsal interoseous, ED extensor digitorum.

Source	Approximate range	Mean ± std
Semmler et al. (2003)		
First DI CIS		
Young subjects	0.13-1.169	0.68 ± 0.42
Old subjects	0.01-2.47	0.76 ± 0.52
Keen and Fuglevand (2004)		
ED CIS		
Same compartment	0-1.6	0.7±0.3
Different compartments	0-1.04	0.4±0.22
Winges and Santello (2004)		
FDP CIS		
Different compartments	0-0.98	0.36±0.21
McIsaac and Fuglevand (2007)		
FDS CIS		
Same compartment	0-1.35	0.45± 0.3
Different compartments	0-0.8	0.23± 0.19
k		
Same compartment	0-1.5	0.63±0.29
Different compartmen	0-1.2	0.42±0.26

for both methods were more widely distributed as p_c increased. For instance, in simulations with p_c around 0.1 the CIS range was 0.05 to 0.65. On the other hand, simulations of p_c was 0.9 resulted in CIS values in the range 0.9 to 2.05 for the cumulative sum method, and 0.7 to 2.2 for the independence method. The slope of the linear fit using the independence method for peak detection was larger than the slope using the cumulative sum method, however, the linear fit using the independence method was always above the fit for the cumulative sum method, especially for smaller values of p_c. This tendency can be explained, in part, by the fact that the cumulative sum method introduces an error in the width of the peak as p_c gets closer to 0, thereby allowing more counts to be admitted in the calculation of the index. In all batches of simulations the linear models for the two indices converged toward a common value as p_c was closer to 1.

Fig. 5.5B shows all the k values obtained from the simulations shown in part A. The overall behavior of k as a function of common input was similar to that displayed by CIS. k also showed a linear, increasing tendency as a function of p_c with a wider range of values as p_c increased. The range of k values was between 0.85 and 2.4 ($k \in [-0.15, 1.4]$). When the k values were compared using different methods for peak detection, the slopes of the linear fit were very similar but the values predicted by the linear model were consistently larger when using the independence method. This could be explained in part because the peak sizes that result from using the correction for independence never involve values that are below the baseline count, as opposed to the cumulative sum method, which occasionally defines peaks containing counts below the base line. The duration of the peaks calculated using the correction for independence are shown in Fig. 5.6 to illustrate the relationship between peak duration and common input. Peak duration as a function of p_c was best described by a linear relationship with positive slope. The number of MN pairs with correlogram peaks lasting less than 10 ms was counted and divided by the total number of simulations. The proportion of pairs with peaks lasting 10 ms or less was 0.55 but importantly, the duration of the peaks increased beyond 10 ms as the proportion of common input increased. The linear prediction from these simulations is that the

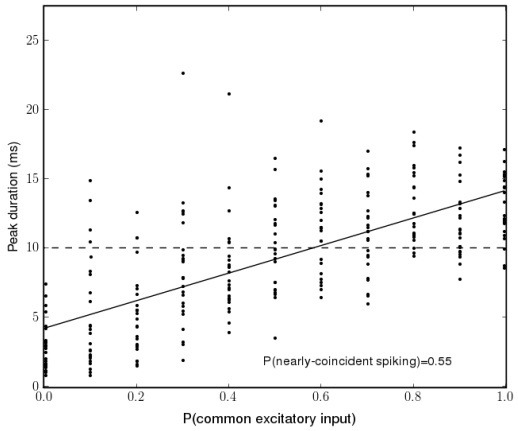

Figure 5.6: Peak duration as a function of p_c using correction for independence.

peak duration will be longer than 10 ms at when the proportion of common inputs is approximately 0.6 or larger.

5.3.2 Nearly-coincident spiking when EPSP amplitudes are different

To assess the how the relationship between the coincidence indices CIS and k and p_c changes with synaptic efficacy, sets of simulations similar to those in subsec. 5.3.1 where the probability of synaptic activation p_s for each input axon contacting a MN was uniformly sampled from the intervals $[0.25, 0.4]$, $[0.4, 0.6]$, and $[0.6, 0.75]$ while keeping other parameters of the model constant ($N_a = 250$, $r \in [10, 50]$, and $0 \leq p_c \leq 1$). That is, three sets of simulations similar to the ones shown in previous paragraphs were performed, the coincidence indices were calculated, and the results were fit using a general polynomial model (Fig. 5.7). In all cases the best fit was linear. The overall tendencies described in the previous section were also displayed for each of the different intervals of p_s considered in this part of the study.

The general tendency for CIS was to increase monotonically with the synaptic efficacy of the inputs for all values of p_c. The difference between CIS values obtained from adjacent synaptic activation intervals (e.g. $p_s \in [0.25, 0.4]$ vs $p_s \in [0.4, 0.6]$) was always positive and became larger as p_c increased. On the other hand, k showed the opposite trend for each value of p_c, in this case the k values decreased with larger synaptic efficacy. The reason for this increase is that the increases in synaptic

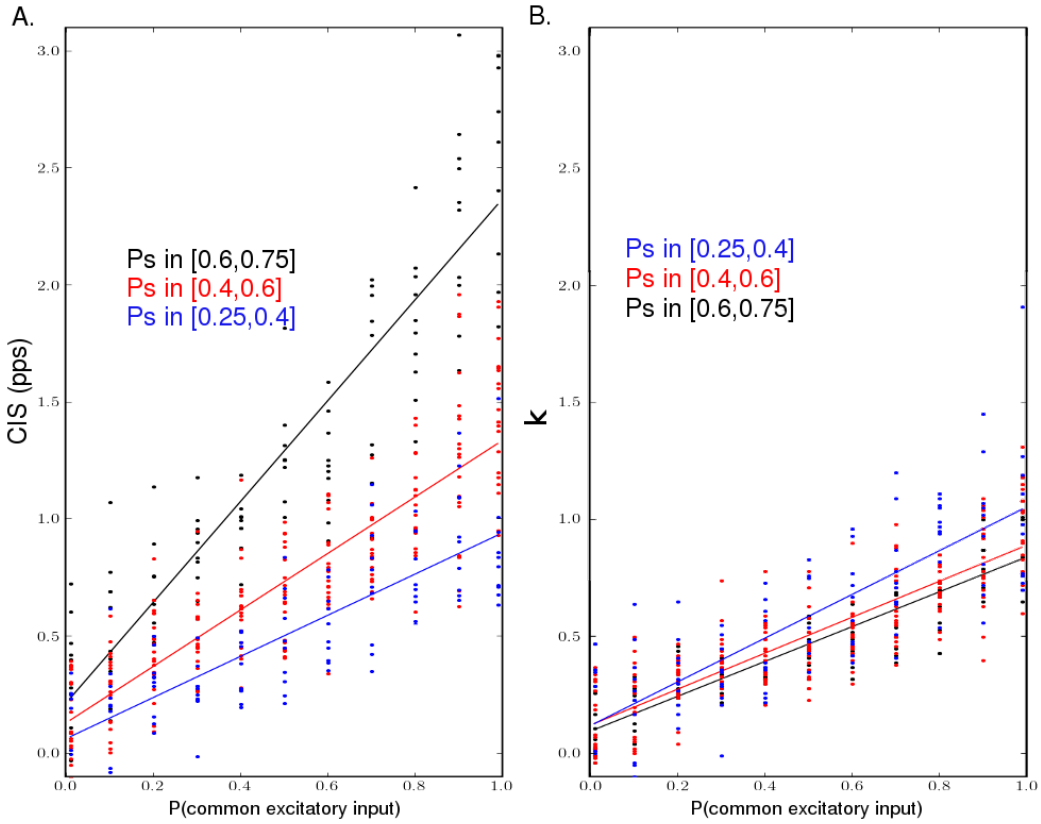

Figure 5.7: Relationship between the indices CIS and k, and synaptic efficacy. The probability of synaptic activation for each input was sampled from the intervals $[0.25, 0.4]$, $[0.4, 0.6]$ and $[0.6, 0.75]$ resulting in average MN firing rates approximately within the intervals $[6, 10]$, $[8, 17]$ and $[12, 22]$ pps. The peak detection was done using Ellaway's cumulative sum method. **A.** CIS. **B.** k.

efficacy resulted in larger peak regions but also in higher baseline counts so that, in general, the baseline count increased slightly more than the peak counts beyond the baseline. The absolute differences between indices for p_s in adjacent intervals were still always larger than zero, and increased for larger values of p_c.

Because k was little affected by changes in the size of composite EPSPs, it is concluded that k is a more robust indicator of common input than CIS with respect to synaptic efficacy.

5.3.3 Nearly-coincident spiking in neurons with statistically different EPSP amplitudes

To investigate the behavior of the two indices CIS and k for *cell pairs in which the synaptic efficacy of the inputs was different*, simulations were carried out by setting the probabilities of synaptic activation for the reference cell to range between 0.1 and 0.75, and between 0.4 and 0.75 for the response cell ($N_a = 250$, $r \in [10, 50]$, and $0 \leq p_c \leq 1$, $N = 203$). This manipulation of the probability of synaptic activation can be thought of as simulating MNs with different recruitment thresholds (Fig. 5.8). The resulting firing rate ranges for the two cells were 4.18 to 13.75 pps for the reference cell, and 13.75 to 19.92 pps for the response cell. The values for both indices of coincidence were lower compared to any of the previous conditions explored so far, with a maximum value of 1.6 for CIS and 1.95 for k ($max(k) = 0.95$).

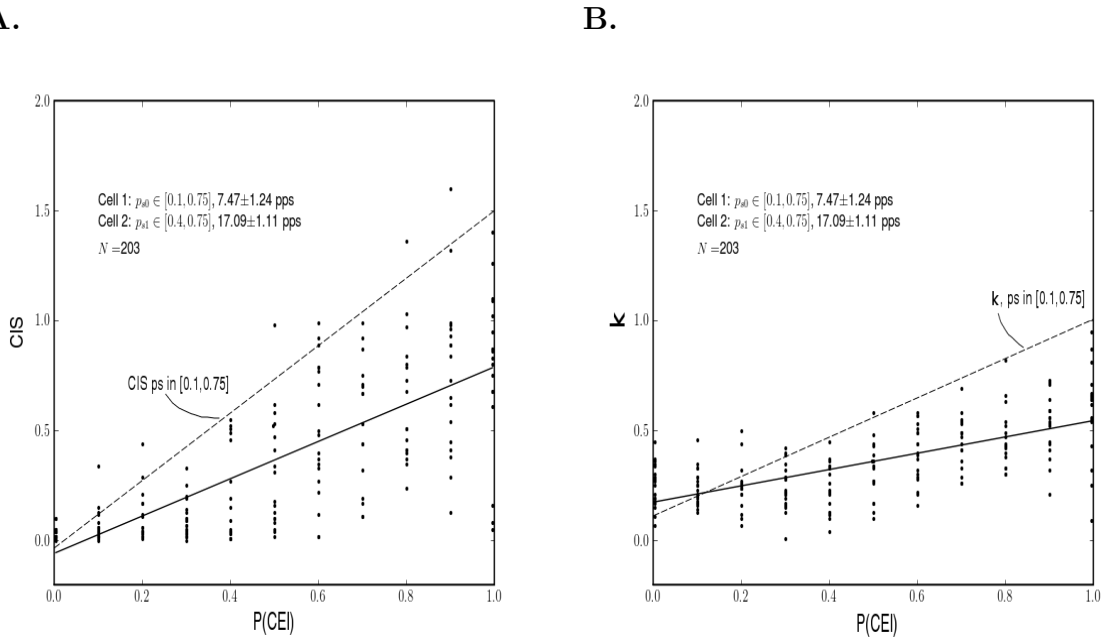

Figure 5.8: Indices of near-coincidence for cell pairs in which the EPSP amplitudes were statistically different. **A.** CIS. **B.** k. The dashed line represents the case in which both neurons had p_s in [0.1,0.75] from Fig. 5.5.

Interestingly, the duration of the nearly-coincident episodes were also smaller (Fig. 5.9). The range of values for the peak duration were 0.13 to 12.93 ms with

mean ± std equal to 4.68 ±3.46 ms, compared to 9 ± 2.9 ms in the case where $p_s \in [0.1, 0.75]$.

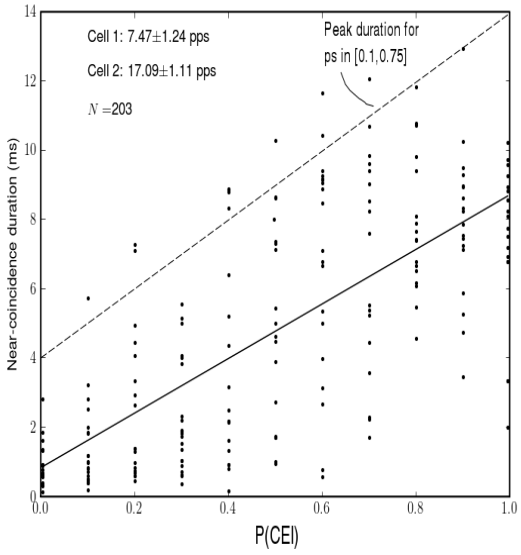

Figure 5.9: Duration of nearly-coincident spiking for pairs of cells in which the probabilities of synaptic activation are statistically different (*e.g.,* EPSP amplitudes are statistically different. The dashed line is the linear fit to the simulations in which both neurons had p_s in [0.1,0.75] from Fig. 5.5.

5.3.4 Nearly-coincident spiking for increasing levels of synaptic drive

The relationship between the indices CIS and k, and p_c was also quantified as the number of input axons increased between 250 and 290, yielding increasingly higher firing rates in the MNs between 8, and 15 approximately, while keeping all other parameters the same ($p_s \in [0.1, 0.75]$, $N_a = 250$, and $0 \leq p_c \leq 1$).

As in previous sections, the tendency for both indices was to increase with p_c regardless of the number of input axons driving the MNs (Fig. 5.10). The general tendency showed by the indices was to display an increase in CIS and a decrease in k for increasing values of N_a for $p_c > 0.4$. There was some crossover between the predicted values of the indices when p_c decreased below 0.4. This crossover effect could be possibly explained by the error introduced in the peak detection for lower values of p_c. In general, the ranges of values taken by the two indices were very similar to those observed in the general case, perhaps with a larger spread in the range of each index for larger p_c.

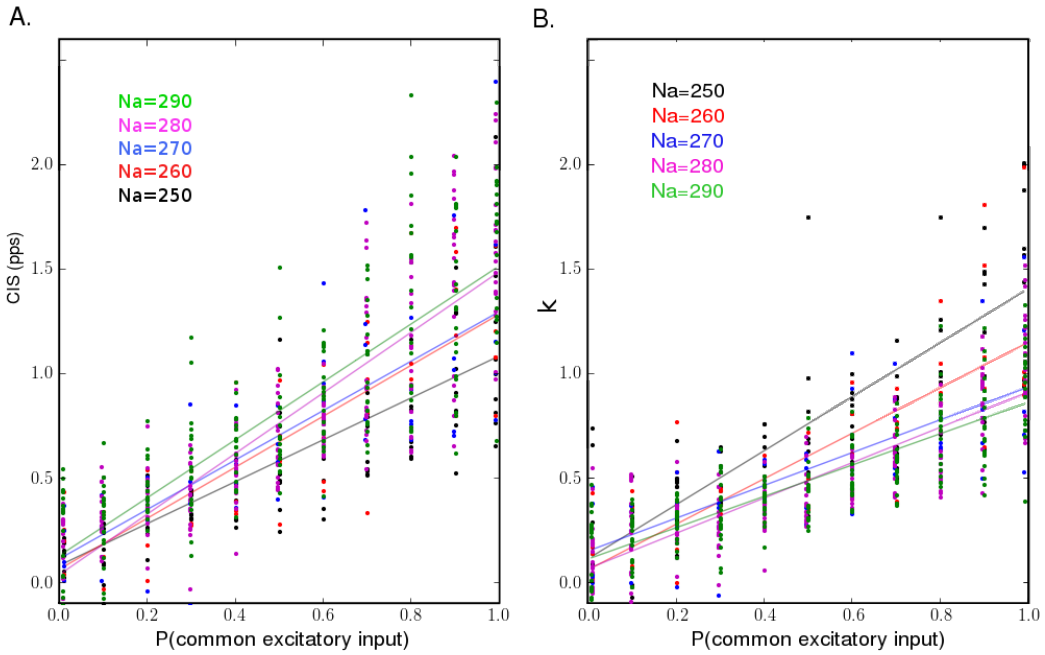

Figure 5.10: Relationship between coincident spiking and the number of input axons. Simulations were done increasing the number of input axons from 250 to 290 resulting in firing rates between 8 and 15 Hz. **A.** CIS **B.** k.

5.4 Simplified model.

Recall that the number of synapses activated by a single axon is different for each input spike. The number of active synapses for an input axon having probability of single synaptic activation p_s can be replaced by its average, $N_s p_s$, where N_s is the maximum number of synapses per axon. The result of making such a substitution is that the size of the EPSPs triggered by input spikes from the same axon will be the same and approximately equal to the average of the composite EPSPs triggered by spikes from the same axon. This simplification decreases the simulation time and importantly, neither the sensitivity of the model to the number of inputs, nor the variability in the spiking of the MNs was affected 5.11. An example showing simulation results using the simplified model is shown in Figure 5.12.

A. B.

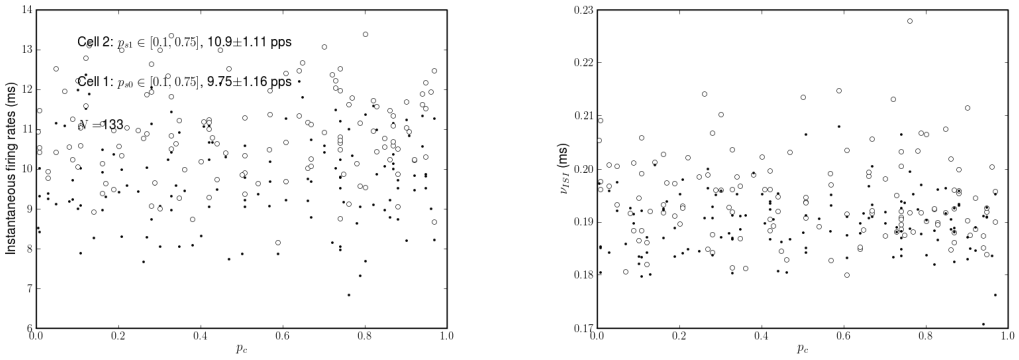

Figure 5.11: Spiking properties of the MNs resulting from simulations assuming that the number of synapses activated by a single axon equals the average number of active synapses in response to input spike from that axon. The average number of synapses for an input axon with probability of single-synapse activation p_s is $N_s p_s$ where N_s is the maximum number of synapses made by an input axon. A. Average firing rates of the neuron pairs simulated. B. Coefficient of variation of the interspike intervals.

5.5 Discussion.

Taken together, these simulation results suggest that it is possible to observe significant nearly-coincident spiking in uncoupled MNs in response to possibly common, but otherwise uncorrelated excitatory synaptic input. The close agreement between the values of CIS and k obtained from the model and those reported experimentally suggest that the model can be used to generate translations from the experimentally obtained indices of nearly-coincident spiking, and percentages of common presynaptic inputs to the motor units under observation. For illustration, a prediction from the model based on the report by Keen and Fuglevand (2004) is that the percentage of common excitatory input to any two MNs supplying the ED muscle ranges between 20% and 70%.

A common observation from all the simulation results obtained thus far is that if the firing rate of the two MNs increases and it is similar, then the duration of the peak and the baseline will increase. The spike counts above the base line increase, but such an increase will be less than the corresponding increase in the baseline counts. As a consequence, then the corresponding indices of nearly-coincident spik-

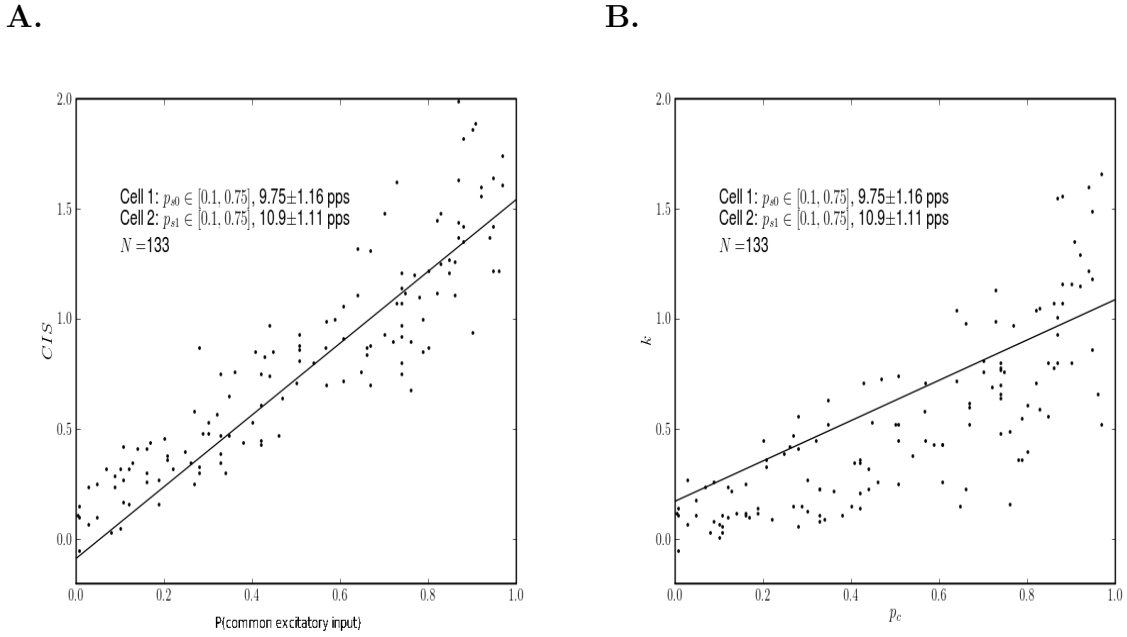

Figure 5.12: Nearly-coincident spiking measured by the indices CIS (**A**) and k (**B**) as a function of the probability of common input p_c for simulations produced by simplified model. See also Figure 5.11

ing will be higher in the case of CIS, and lower for k, as shown by the simulations in which p_n and N_a were systematically increased (Figs. 5.7 and 5.10). In contrast, if the firing rates of the two neurons were not similar, the two indices CIS and k decreased for all the levels of common input (Fig. 5.8) in simulations where p_n and N_a were varied. The reasons underlying this result are currently being investigated. The statistics of the interspike intervals might play an important role in shaping the relationship between the firing rates and the nearly-coincident spiking of two neurons.

The results obtained with our simulations are different from those of other investigators (Binder and Powers, 2001; Taylor and Enoka, 2004; Lowery and Erim, 2005) in two fundamental ways. First, the values for the CIS and k indices were in agreement with experimentally reported values for all conditions tested here from the outset and without furter exploration of the parameter space. Other investigators have reported index values that agree with experimental data only for a

restricted set from several initial conditions explored. The reasons for the agreement with experimental data reported here might include the fact that the MN models were constructed without including any parameters that had not been experimentally measured (*e.g.,* dendritic length, distribution of active properties in dendrites, equivalent cylinder reductions of dendritic trees). Instead, the MN models constructed here focused on controlling different schemes of connectivity based on well characterized responses recorded at the soma of MNs and the output properties of the cells were calibrated using results obtained from recordings of motor units controlling upper limb muscles. One major difference between the model presented here and others is that synaptic input is simulated using EPSPs triggered by separate input neurons, assuming that each input axon makes multiple synaptic contacts, each with a certain probability of releasing neurotransmitter. The composite EPSPs resulting from such assumptions can have peak amplitudes of up to 1.4 mV, which is larger than one order of magnitude in comparison to the single-synapse somatic EPSPs, reaching peak amplitudes of approximately 150 μV. This feature turned out to be crucial in the implementation of the model and in the output spiking of the MN simulations, as indicated by the behavior of the firing rates and the coefficients of variation of the interspike intervals. One of the reasons is that larger composite EPSP sizes increase the standard deviation of the membrane potential, eventually decreasing the standard deviation of the interspike intervals. If the firing rate is kept constant by making appropiate changes in the number of inputs or their firing rates, the coefficient of variation of interspike intervals will decrease for larger EPSP amplitudes.

The relationship between the indices of coincidence and the proportion of common input was best fit by a linear model in our simulations, as opposed to an exponential, if not sigmoidal fits reported in other models (Binder and Powers, 2001; Taylor and Enoka, 2004). None of the previous studies have incorporated realistic synaptic input in the form of single EPSPs triggered at high frequency from different sources. Instead, other researchers have simulated the common inputs either by injecting filtered current signals that mimmic synaptic noise to neurons, independently

of the membrane potential (Binder and Powers, 2001; Lowery and Erim, 2005), or by triggering EPSPs at high frequency using a single Poisson process to represent all the input spikes instead of several independent sources (Taylor and Enoka, 2004) (which yields completely different distributions for the input spike counts).

The high degree of variability in CIS or k values at any given level of common input, specially for the largest values of p_c (Fig. 5.5) highlights the importance of obtaining many samples of CIS or k in order to obtain a reasonable estimate of common input. Note that although the indices CIS and k have different metrics, the difference between mean values of CIS for $p_c = 0$ and $p_c = 1.0$ was larger than for the corresponding k values in each of the conditions tested here. The variability of the values for k was also smaller than for CIS. It is worthwhile to keep in mind that the probability of error in selecting a level of common input given an index value using the regression lines showed in Figs. 5.5-5.10 decreases if the index is itself less variable. On the basis of the simulations presented here, the smaller variability of the index k compared to CIS suggests that k is a more robust index to quantify nearly-coincident spiking than CIS.

In addition, the modification to the method of peak detection introduced here now allows the quantification of the duration of nearly-coincident spiking episodes. It is worth notice, however, that the way peaks are being detected induces a positive bias in both indices near $p_c = 0$ since only positive deflections from the predicted count of independent spikes are taken into account to calculate the peak. The positive bias could wrongly be interpreted as presence of common input when there is actually none. Two possible ways in which the current methodology of assessing nearly-coincident spiking could improve to deduce levels of common input involve (1) introducing a measure of significance for deflections above the base-line predicted by independent spiking in the method used here, and (2) counting cross- interspike intervals by measuring the delays between spikes in the response cell that occur after spikes in the reference cell only if there were no other spikes in between. These possibilities are being currently assessed and tested for their future implementation.

Chapter 6

Summary and conclusions.

6.1 Summary

Experimental evidence about the behavior of motor neurons from the cellular to the systems perspective was combined with stochastic and deterministic mathematics to produce a spiking model of spinal MNs receiving realistic excitatory synaptic input. The model was constructed taking care to use only well established evidence and parameter ranges for biophysical variables. The rules governing the dynamics of the membrane potential were derived using dynamical systems theory taking into account the behavior of MNs observed in experimental conditions both *in vitro* and *in vivo*. The model parameters were adjusted to describe, as faithfully as possible, the biophysical processes that lead to spike generation in real neurons. The result of this process was a tractable, realistic model that allows the study of joint spiking in MNs.

The *primary findings* and predictions of this work are summarized in the following paragraphs.

The MN model constructed here reproduce previously documented properties of MNs. The model predicts that the minimum number of active excitatory inputs necessary to drive the MN firing to rates similar to those observed experimentally is between 200 and 450 depending on the distribution of somatic, composite EPSP amplitudes (*e.g.,* different input resistances). The interspike interval variation of the model MNs agrees with *in vivo* observations from motor unit recordings. Realistic common excitatory synaptic input into MNs is sufficient to produce nearly-coincident spiking for very low proportions of common excitatory input.

One of the most important findings of this work is that, in simulations of simultaneous MN activity receiving different levels of excitatory common synaptic

input, the values for the indices CIS and k of nearly-coincident spiking overlap with experimentally measured values. The simulations produced here allow us to go back to previously recorded motor units and reinterpret the results in terms of common synaptic input, enabling the estimation of potential schemes of presynaptic connectivity into different kinds of MNs.

The indices of nearly-coincident spiking CIS and k increase as a function of common excitatory input (Fig. 5.5).

For a given level of common excitatory input, if the firing rates of the two neurons are similar, CIS is expected to increase, and k is expected to decrease in response to an increase in firing rate in the pair of motor neurons. This point is illustrated in Figs. 5.7 and 5.10.

In contrast, if the firing rates of the two neurons are different, the model predicts smaller values for both indices, at any given level of common input. Simulations were MNs pairs where one of the MNs was more likely to spike were performed to illustrate this point (Fig. 5.8).

The simulations highlight the importance of taking samples of simultaneous motor unit activity to calculate the indices of near-coincidence. The simulations show that there is a bias toward positive values in the calculation of the CIS and k indices for proportions of common input close to 0. These observations suggest that motor unit data containing positive, but low CIS and k values obtained experimentally that were previously interpreted as indicative of common presynaptic input to motor units should be review and reinterpreted.

The construction of the model included only independent excitatory input to uncoupled MNs allowed the study of nearly-coincident spiking as a result of common synaptic input only. However, such assumptions may also constitute a limitation of the modeling approach taken here since MNs receive other sources of synaptic input that include inhibitory synaptic input. In addition, polysynaptic coupling of the MNs and their sources may also influence the joint spiking activity in MNs. A future direction of the work started in this dissertation is a systematic expansion of the model presented here so that different sources of synaptic input and connectivity are

taken into account. The anatomical and physiological data available to date partially justifies the approach taken here (see Chapter 2) and the input-output properties of the motor neurons are in good agreement with experimental data. Taken together, these last two observations validate the results presented here. Future studies that include more complex networks of MNs and their inputs can be constructed based on this first approach, designed to be a footstep in a series of theoretical studies relating motor unit behavior to the network connectivity in the motor system.

The model enables its user to test different hypotheses about synaptic efficacy, synaptic innervation, firing characteristics of cells presynaptic to MNs, and intrinsic properties of the MN membranes, by varying pre- and postsynaptic parameters like the probability of single synapse activation, the number of synapses per axon, the total number of inputs to MNs and the firing rates of the input cells. One important prediction from the model that agrees with previous estimates is that the number of axons necessary to drive a MN to fire at rates comparable to those experimentally observed in motor units recorded from intact animals is approximately between 220 and 450 (Kernell, 2006). Importantly, this prediction relies on another estimate that also agrees with predictions based on anatomical and physiological observations, that the number of synapses made by an input axon onto a MN is between 10 and 12 (Kernell, 2006). Using these ranges, the other parameters of the model can be adjusted to match the output produced by experimentally recorded MNs and make inferences about the percentage of common excitatory input they receive.

The model can also be useful to interpret existing data recorded from motor neurons, or units, innervating the same or different muscles, for different conditions such as during development (see Semmler et al. (2003)) or training (Semmler et al., 2004), and generate hypotheses to explain putative differences in the joint activity of motor unit pairs on the basis of their presynaptic innervation. For example, the data comparing motor units from young and older subjects from Semmler et al. (2003) suggests that the percentage of common inputs to MNs belonging to the young individuals could be up to 20% less than for the older subjects. In another example, this time regarding data from human motor units, the model predicts that

the maximum common excitatory input to pairs innervating the same compartment of extensor digitorum can be, depending on the firing rates of the recorded units, between 20 and 30% larger than the common excitatory input to units innervating the same compartment of flexor digitorum superficialis (resp. Keen and Fuglevand, 2004; McIsaac and Fuglevand, 2007). The model can also be used to establish an *a priori* functional comparison of connectivity schemes of presynaptic input to MNs across different species, in particular for different primates (see Nakajima et al., 2000). Similarly, the model could be implemented in the clinical setting to evaluate the recovery of patients with partial spinal cord lesions based on the simultaneous motor unit activity recorded from muscles innervated by motor units below and above the lesion locations (Farmer et al., 1993).

In sum, the model allows the manipulation of variables related synaptic connectivity and to simulate output behavior that can be analyzed in the conventional approach taken in experimental work. In consequence, one of the important outcomes of this modeling effort is a quantitative means to link measures of nearly coincident spiking with plausible representations of synaptic connectivity. Specifically, the remarkable similarity of the index values obtained from simulations with experimental data allows an *a priori* estimation of the number of last order branched inputs to motor units recorded *in vivo*.

REFERENCES

Adams, L., A. Datta, and A. Guz (1989). Synchronization of motor units firing during different respiratory and postural tasks in human sternocleidomastoid muscle. *J. Physiol.*, **413**, pp. 213–231.

Ali, A. B., J. Deuchars, H. Pawelzik, and A. M. Thomson (1998). CA1 pyramidal to basket and bistratified cell EPSPs: dual intracellular recordings in rat hippocampal slices. *J. Physiol.*, **507**, pp. 201–207.

Asanuma, H., P. Zarzecki, E. Jankowska, T. Hongo, and S. Marcus (1979). Projection of individual pyramidal tract neurons to lumbar motor nuclei of the monkey. *Experimental Brain Research*, **34**, pp. 73–89.

Av-Ron, E., H. Parnas, and L. A. Segel (1993). A basic biophysical model for bursting neurons. *Biological Cybernetics*, **69**, pp. 87–95.

Baker, J., F. Bremner, J. Cole, and J. Stephens (1987). Short-term synchronization of intrinsic hand muscle motor units in a deafferented man. *J. Physiol.*, **396**, p. 155P.

Baldissera, F., H. Hultborn, and M. Illert (1981). *In Handbook of Physiology. The Nervous System. Motor Control.*, volume II, section 1, part 2, chapter Integration in spinal neuronal systems, pp. 509–595. Am. Physiol. Soc., Bethesda, MD.

Bawa, P. and B. Calancie (1983). Repetitive doublets in human flexor carpi radialis muscle. *J. Physiol.*, **339**, pp. 123–132.

Binder, M. D. and R. K. Powers (2001). Relationship between simulated common synaptic input and discharge synchrony in cat spinal motoneurons. *J. Neurophysiol.*, **86**, pp. 2266–2275.

Bremner, F., J. Baker, and J. Stephens (1991a). Correlation between the discharges of motor units recorded from the same and from different finger muscles in man. *J. Physiol.*, **432**, pp. 355–380.

Bremner, F., J. Baker, and J. Stephens (1991b). Variation in the degree of synchronization exhibited by motor units recorded from the same and from different finger muscles in man. *J. Physiol.*, **432**, pp. 381–399.

Brody, C. D. (1999a). Correlations without synchrony. *Neural Computation*, **11**, pp. 1537–1551.

Brody, C. D. (1999b). Disambiguating between different covariation types. *Neural Computation*, **11**, pp. 1527–1535.

Burke, R. E. (1967). Composite nature of the monosynaptic excitatory postsynaptic potential. *J. Neurophysiol.*, **30**, pp. 1114–1137.

Calvin, W. H. and P. C. Schwindt (1972). Steps in production of motoneuron spikes during rhythmic firing. *J. Neurophysiol.*, **35**, pp. 297–310.

Cheney, P. D. and E. E. Fetz (1980). Functional classes of primate corticomotoneuronal cells and their relation to active force. *J. Neurophysiol.*, **44**, pp. 773–791.

Connel, L., N. Davey, and P. Ellaway (1986). The degree of short-term synchrony between α- and γ-motoneurones coactivated during the flexion reflex in the cat. *J. Physiol.*, **376**, pp. 47–61.

Cox, D. R. (1962). *Renewal Theory.* John Wiley & Sons, Inc., New York.

Datta, A., S. Farmer, and J. Stephens (1991). Central nervous pathways underlying synchronization of human motor unit firing studied during voluntary contractions. *J. Physiol.*, **432**, pp. 401–425.

Datta, A. and J. Stephens (1990). Synchronization of motor unit activity during voluntary contraction in man. *J. Physiol.*, **422**, pp. 397–419.

de la Rocha, J., B. Doiron, E. Shea-Brown, K. Josic, and A. Reyes (2007). Correlation between neural spike trains increases with firing rate. *Nature*, **448**, pp. 802–807.

Dietz, V., E. Bischofberger, C. Wita, and H. Freund (1976). Correlation between the discharges of two simultaneously recorded motor units and physiological tremor. *Electroencephalogr. Clin. Neurophysiol.*, **40**, pp. 97–105.

Ellaway, P. (1978). Cumulative sum technique and its application to the analysis of peristimuls time histograms. *Electroencephalogr. Clin. Neurophysiol.*, **45**, pp. 302–304.

Ellaway, P. and K. Murthy (1985). The origins and characteristics of cross-correlated activity between γ-motoneurones in the cat. *Quarterly Journal of Experimental Physiology*, **70**, pp. 219–232.

Endresen, L. P., K. Hall, J. S. Hoye, and J. Myrheim (2000). A theory for the membrane potential of living cells. *European Journal of Biophysics*, **29**, pp. 90–103.

Ermentrout, B. G. and N. K. Kopell (1998). Fine structure of neural spiking and synchronization in the presence of conduction delays. *Proc. Natl. Acad. Sci.*, **95**, pp. 1259–1264.

Farmer, S., M. Swash, D. Ingram, and J. Sthephens (1993). Changes In Motor Unit Synchronization Following Central Nervous Lesions In Man. *J. Physiol.*, **463**, pp. 83–105.

Fitz-Hugh, R. (1961). Impulses and physiological states in theoretical models of nerve membrane. *Biophysical Journal*, **1**, pp. 445–466.

Garland, S. and T. Miles (1997). Control of motor units in human flexor digitorum profundus under different propioceptive conditions. *J. Physiol.*, **502**, pp. 693–701.

Gibbs, J., L. Harrison, and J. Stephens (1995). Organization of inputs to motoneurone pools in man. *J. Physiol.*, **485**, pp. 245–256.

Gilchrist, L. S. and K. A. Mesche (1997). Coactivation of putative octopamine- and serotonin-containing interneurons in the medicinal Leech. *J. Neurophysiol.*, **78**, pp. 2108–2115.

Granit, R., D. Kernell, and S. GK (1963). Quantitative aspects of repetitive firing of mammalian motoneurones, caused by injected currents. *J. Physiol.*, **168**, pp. 911–931.

Heeger, D. (2000). Spike trains and renewal processes.

Herrera-Valdez, M. A. and J. Lega (2008a). A biophysical and computationally efficient model of membrane potential for excitable cells. *In preparation, PDF-link.*

Herrera-Valdez, M. A. and J. Lega (2008b). A simple, generic, and physiologically significant model for the pacemaker dynamics of cardiac cells. *In preparation, PDF-link.*

Hockensmith, G. B., S. Y. Lowell, and A. Fuglevand (2005). Common input across motor nuclei mediating precision grip in humans. *J. Neuroscience*, **25(18)**, pp. 4560–4564.

Hodgkin, A. and A. Huxley (1952). A quantitative description of membrane current and its application to conduction and excitation in nerve. *J. Physiol.*, **117**, pp. 500–544.

Izhikevich, E. (2007). *Dynamical Systems in Neuroscience.* MIT, MIT Press, 55 Hayward Street, Cambridge MA 02142.

Izhikevich, E. M. (2003). Simple Model of Spiking Neurons. *IEEE Transactions on Neural Networks*, **14(6)**, pp. 1569–1572.

Izhikevich, E. M. (2004). Which model to use for cortical spiking neurons. *IEEE Transactions on Neural Networks*, **15(5)**, pp. 1063–1070.

Jack, J., S. Redman, and K. Wong (1981). The components of synaptic potentials evoked in cat spinal motoneurones by impulses in single group Ia afferents. *J. Physiol.*, **321**, pp. 65–96.

Jankowska, E. (1992). Interneuronal relay in spinal pathways from propioceptors. *Prog. Neurobiol.*, **38**, pp. 335–378.

Jankowska, E., Y. Padel, and R. Tanaka (1975). Projections of pyramidal tract cells to alpha-motoneurones innervating hind-limb muscles in the monkey. *The Journal of Physiology*, **249**(3), pp. 637–67. ISSN 0022-3751. doi:1177109. PMID: 1177109.

Jankowska, E. and W. J. Roberts (1972). Synaptic actions of single interneurones mediating reciprocal Ia inhibition of motoneurones. *The Journal of Physiology*, **222**(3), pp. 623–42. ISSN 0022-3751. doi:5033026. PMID: 5033026.

Johnston, R., C. Consulas, H. Pfl´uuger, and R. B. Levine (1998). Patterned activation of unpaired median neurons during fictive crawling in *Manduca sexta* larvae. *Journal of experimental biology*, **202**, pp. 103–113.

Kandel, E. R., J. H. Schwartz, and T. H. Jessell (2000). *Principles of Neuroscience*. McGraw-Hill.

Keen, D. and A. Fuglevand (2004). Common input to motor neurons innervating the same and different compartments of the human extensor digitorum muscle. *J. Neurophysiol.*, **91**, pp. 57–62.

Kernell, D. (1965a). The adaptation and the relation between discharge frequency and current strenght of cat lumbosacral motoneurones stimulated by long-lasting injected currents. *Acta Physiologica Scandinavica*, **65**, pp. 65–73.

Kernell, D. (1965b). The limits of firing frequency in cat lumbosacral motoneurones processing different time course of afterhyperpolarization. *Acta Physiologica Scandinavica*, **65**, pp. 87–100.

Kernell, D. (1965c). Synaptic influence on the repetitive activity elicited in cat lumbosacral motoneurones by long-lasting injected currents. *Acta Physiologica Scandinavica*, **63**, pp. 409–410.

Kernell, D. (2006). *The Motoneurone and its Muscle Fibres*. Oxford, Great Clarendon Street, Oxford OX2 6DP.

Kirkwood, P. (1979). On the use and interpretation of cross-correlation measurements in the mammalian central nervous system. *J. Neuroscience Methods*, **1**, pp. 107–132.

Kirkwood, P. and T. Sears (1978). The synaptic connections to intercostal motoneurones as revealed by their average common excitatory potential. *J. Physiol.*, **275**, pp. 103–134.

Kirkwood, P., T. Sears, D. Tuck, and R. Westaard (1982a). Variations in the time course of synchronization of intercostal motoneurones in the cat. *J. Physiol.*, **327**, pp. 105–135.

Kirkwood, P., T. Sears, and R. Westgaard (1982b). Restoration of function in external intercostal motoneurones in the cat following partial central deafferentation. *J. Physiol.*, **327**, pp. 105–135.

Kopell, N. K., B. G. Ermentrout, M. Whittington, and R. Traub (2000). Gamma rhythms and beta rhythms have different synchronization properties. *Proc. Natl. Acad. Sci. USA*, **97**, pp. 1807–1872.

Kuhn, A., A. Aersten, and S. Rotter (2004). Neuronal integration of synaptic input in the fluctuation-driven regime. *J. Neuroscience*, **24(10)**, pp. 2345–2356.

Kumar, A., S. Rotter, and A. Aersten (2008). Conditions for propagating synchronous spiking and asynchronous firing rates in a cortical network model. *J. Neuroscience*, **28(20)**, pp. 5268–5280.

Lawrence, D., R. Porter, and S. Redman (1985). Corticomotoneuronal synapses in the monkey: Light microscopic localization upon motoneurons of intrinsic muscles in the hand. *J. Comp. Neurology*, **232**, pp. 499–510.

Lowery, M. M. and Z. Erim (2005). A simulation to examine the effect of common motoneuron inputs on correlated patterns of motor unit discharge. *J. Computational Neuroscience*, **19**, pp. 107–124.

Markowitz, D. A., F. Collman, C. D. Brody, J. J. Hopfield, and D. W. Tank (2008). Rate specific synchrony: Using noisy oscillations to detect equally active neurons. *Proc. Natl. Acad. Sci.*, **105**, pp. 8422–8427.

McIsaac, T. L. and A. J. Fuglevand (2007). Motor unit synchrony within and across compartments of the human flexor digitorum superficialis. *J. Neurophysiol.*, **97**, pp. 550–556.

Mendell, L. M. and E. Henneman (1971). Terminals of single Ia fibers: location, density, and distribution within a pool of 300 homonymous motoneurons. *Journal of Neurophysiology*, **34**(1), pp. 171–87. ISSN 0022-3077. doi:5540577. PMID: 5540577.

Mochizuki, G., T. Ivanova, and S. Garland (2005). Synchronization of motor units in human soleus muscle during standing postural tasks. *J. Neurophysiol.*, **94**, pp. 62–69.

Morris, C. and H. Lecar (1981). Voltage oscillations in the barnacle giant muscle fiber. *Biophysical Journal*, **35**, pp. 193–213.

Nakajima, K., M. Maier, P. Kirkwood, and R. Lemon (2000). Striking differences in transmission of corticospinal excitation to upper limb motoneurons in two primate species. *J. Neurophys.*, **84**, pp. 698–709.

Nielsen, J., B. Conway, D. Halliday, M.-C. Perreault, and H. Hultborn (2005). Organization of common synaptic input drive to motor neurons during fictive locomotion in the spinal cat. *J. Physiol.*, **569.1**, pp. 291–304.

Nordstrom, M., A. J. Fuglevand, and R. Enoka (1992). Estimating the strength of common input to human motoneurons from the cross-correlogram. *J. Physiol.*, **453**, pp. 547–574.

Nykamp, D. Q. (2003). Spike correlation measures that eliminate stimulus effects in response to white noise. *J. Computational Neuroscience*, **14**, pp. 193–209.

Penfield, W. and E. Boldrey (1937). Somatic motor and sensory representation in the cerebral cortex of man as studied by electrical stimulation. *Brain: A Journal of Neurology*, **60**, pp. 389–443.

Perkel, D., G. Gerstein, and G. P. Moore (1967a). Neuronal spike trains and stochastic point processes I. The Single Spike Train. *Biophysical Journal*, **7**, pp. 391–418.

Perkel, D., G. Gerstein, and G. P. Moore (1967b). Neuronal spike trains and stochastic point processes II. Simultaneous spike trains. *Biophysical Journal*, **7**, pp. 419–440.

Perlmutter, S. I., M. A. Maier, and E. D. Fetz (1998). Activity of spinal interneurons and their effects on forearm muscles during voluntary wrist movements in the monkey. *J. Neurophysiol.*, **80**, pp. 2475–2494.

Person, R. S. and L. P. Kudina (1972). Discharge frequency and discharge pattern of human motor units during voluntary contraction of muscle. *Electroencephalography and Clinical Neurophysiology*, **32**(5), pp. 471–83. ISSN 0013-4694. doi:4112299. PMID: 4112299.

Piotrkiewicz, M. (1999). An influence of afterhyperpolarization on the pattern of motoneuronal rhythmic activity. *Journal of Physiology, Paris*, **93**(1-2), pp. 125–33. ISSN 0928-4257. doi:10084716. PMID: 10084716.

Porter, R. and R. Lemon (1993). *Coticospinal function and voluntary movement*. Oxford Science Publications.

Powers, R. K. and M. D. Binder (2000). Relationship between the time course of the afterhyperpolarization and discharge variability in cat spinal motoneurones. *The Journal of Physiology*, **528 Pt 1**, pp. 131–50. ISSN 0022-3751. doi:11018112. PMID: 11018112.

Redman, S. and B. Walmsley (1983a). Amplitude fluctuations In synaptic potentials evoked in cat spinal motoneurons at identified group Ia synapses. *J. Physiol.*, **343**, pp. 135–145.

Redman, S. and B. Walmsley (1983b). The time course of synaptic potentials evoked in cat spinal motoneurones identified at group Ia synapses. *J. Physiol.*, **343**, pp. 117–133.

Romo, R. and E. Salinas (1999). Sensing and deciding in the somatosensory system. *Current Opinion in Neurobiology*, **9**, pp. 487–493.

Schmied, A., C. Ivarsson, and E. Fetz (1993). Short-term synchronization of motor units in human extensor digitorum communis muscle: relation to contractile properties and voluntary control. *Exp. Brain Res.*, **97(1)**, pp. 159–172.

Sears, T. and D. Stagg (1976). Short-term synchronization of intercostal motoneurone activity. *J. Physiol.*, **263**, pp. 357–381.

Segev, I., J. James W. Fleshman, and R. E. Burke (1990). Computer simulation of group Ia EPSPs using morphologically realistic models of cat α-motoneurons. *J. Neurophysiol.*, **64(2)**, pp. 618,660.

Semmler, J., K. Kornatz, D. Dinenno, S. Zhou, and R. Enoka (2002). Motor unit synchronization is enhanced during slow lengthening contractions of a hand muscle. *J. Physiol.*, **545**, pp. 681–695.

Semmler, J. G., K. W. Kornatz, and R. M. Enoka (2003). Motor unit coherence during isometric contractions is greater in a hand muscle of older adults. *J. Neurophysiol.*, **90**, pp. 1346–349.

Semmler, J. G. and M. A. Nordstrom (1995). Influence of handedness on motor unit discharge properties and force tremor. *Experimental Brain Research.*, **104**(1), pp. 115–25. ISSN 0014-4819. doi:7621929. PMID: 7621929.

Semmler, J. G., M. V. Sale, F. G. Meyer, and M. Nordstrom (2004). Motor unit coherence and its relation with synchrony are influenced by training. *J. Neurophysiol.*, **92**, pp. 3320–3331.

Shapavalov, A., O. Karamjan, G. Kurchavyi, and Z. Repina (1971). Synaptic actions evoked from the red nucleus on the spinal alpha-motoneurons in the rhesus monkey. *Brain Research*, **32(2)**, pp. 325–348.

Shinoda, Y., J.-I. Yokota, and T. Futami (1981). Divergent projection of individual corticospinal axons to motoneurons of multiple muscles in the monkey. *Neuroscience Letters*, **23**, pp. 7–12.

Softky, W. and C. Koch (1993). The highly irregular firing of cortical cells is inconsistent with temporal integration of random EPSPs. *J. Neuroscience*, **13**, pp. 334–350.

Taylor, A. M. and R. M. Enoka (2004). Quantification of the factors that influence discharge correlation in model motor neurons. *J. Neurophysiol.*, **91**, pp. 796–814.

Walmsley, B., F. Edwards, and D. Tracey (1988). Nonuniform release probabilities underlie quantal synaptic transmission at a mammalian excitatory central synapse. *J. Neurophysiol.*, **60(3)**, pp. 889–908.

Winges, S. and M. Santello (2004). Common input to motor units of digit flexors during multi-digit grasping. *J. Neurophysiol.*, **92**, pp. 3210–3220.

Yao, W., A. J. Fuglevand, and R. M. Enoka (2000). Motor unit synchronization increases EMG amplitude and decreases force steadiness of simulated contractions. *J. Neurophysiol.*, **83**, pp. 441–452.